UNIVERSIDADE FEDERAL FLUMINENSE

INSTITUTO DE GEOCIÊNCIAS

DEPARTAMENTO DE GEOLOGIA E GEOFÍSICA

PROGRAMA DE PÓS-GRADUAÇÃO EM DINÂMICA DOS OCEANOS E DA TERRA

ELOÍSE HELENA POLICARPO NEVES

MAPPING OF ILHA DO MEL AND PRAIA GRANDE IMPACT STRUCTURES, SANTOS BASIN, THROUGH THE APPLICATION OF SEISMIC ATTRIBUTES

NITERÓI – RJ, BRAZIL

2026

ELOÍSE HELENA POLICARPO NEVES

MAPPING OF ILHA DO MEL AND PRAIA GRANDE IMPACT STRUCTURES, SANTOS BASIN, THROUGH THE APPLICATION OF SEISMIC ATTRIBUTES

Thesis submitted to the Graduate Program in Ocean and Earth Dynamics at Fluminense Federal University in partial fulfillment of the requirements for the degree of Doctor of Philosophy
Area of concentration: Geosciences

Advisor: Dr. Prof. Antonio Fernando Menezes Freire

NITERÓI – RJ, BRAZIL
2026

Ficha catalográfica automática - SDC/BIG
Gerada com informações fornecidas pelo autor

N511m Neves, Eloíse Helena Policarpo
Mapping of Ilha do Mel and Praia Grande impact structures, Santos Basin, through the application of seismic attributes / Eloíse Helena Policarpo Neves. - 2026.
86 f.: il.

Orientador: Antonio Fernando Menezes Freire.
Tese (doutorado)-Universidade Federal Fluminense, Instituto de Geociências, Niterói, 2026.

1. Estruturas de impacto. 2. Atributos sísmicos. 3. Bacia de Santos. 4. Produção intelectual. I. Freire, Antonio Fernando Menezes, orientador. II. Universidade Federal Fluminense. Instituto de Geociências. III. Título.

CDD - XXX

Bibliotecário responsável: Debora do Nascimento - CRB7/6368

MAPPING OF ILHA DO MEL AND PRAIA GRANDE IMPACT STRUCTURES, SANTOS BASIN, THROUGH THE APPLICATION OF SEISMIC ATTRIBUTES

ELOÍSE HELENA POLICARPO NEVES

Thesis submitted to the Graduate Program in Ocean and Earth Dynamics at Fluminense Federal University in partial fulfillment of the requirements for the degree of Doctor of Philosophy

Approval date: April 8, 2026.

THESIS COMMITTEE

_____

Prof. Dr. Antonio Fernando Menezes Freire (Advisor – UFF)

_____

Prof. Dr. Cleverson Guizan Silva (Member – UFF)

_____

Prof. Dr. Wagner Moreira Lupinacci (Member – UFF)

_____

Prof. Dr. Victor Matheus Joaquim Salgado Campos (Member – UFF)

_____

Dr. Ricardo Jahnert (Member – Independent Consultant)

_____

Dr. Roberto Salvador Francisco d'Ávila (Member – Petrobras)

ACKNOWLEDGMENTS

I would like to thank Fernando Freire for his guidance, empathy, and patience throughout this research work.

I would like to thank the members of the examination committee for their time and valuable feedback, which contributed to the scientific development of this work: Cleverson Guizan, Ricardo Jahnert, Roberto D'Ávila, Victor Salgado and Wagner Lupinacci.

I am grateful to CAPES for the scholarship that funded my PhD journey.

I also thank Alvaro Crosta for being a reference in this field and for sharing his articles.

Special thanks to Zoraida Piedade for all her help and patience; her friendship was essential for the completion of this work.

I would like to thank Bruna Maia, Danielle Schemiko, Bruno Rocha, Joao Pedro Reis and Mario Martins for their essential help in this work.

To my dear friends at GIECAR for all the moral support, conversations, coffees, and laughter shared. I hope I do not forget anyone: Ana Carla and Ana Carius for their encouragement and support during my presentations, Bijani for the feedback after Academic Week, Bruna Silva for her partnership at the beginning of my PhD, Mirnis for assistance in fault interpretations, Nadir for the delicious food from Para, Tess for support with Paleoscan, and Ana Moreira, Barbara, Breno, Davy, Francisco, Filipe, Gisela, Hellen, Isabela, Isadora, Jennifer, Jessica, Joana, Jordan, Joyce, Karen, Kenji, Laisa, Leonardo, Maira, Mallet, Marcelly, Nilo, Paula, Pedro, Priscila, Sarah, Tone and Vanessa.

I would like to thank Otaviano from Petrobras for his feedback after a GIECAR Workshop.

I also thank Raissa Siqueira, Ammir, Duda and Ursula from GISIS for their support.

To my family, for all their help and encouragement. Special thanks to all the female professors in my family for their great inspiration and support: MSc. Denise Policarpo, Eliani Policarpo, Dra. Gisele Campos Neves, Dra. Maria Elizabeth Zucolotto, and Dra. Tatiana Campos Neves.

To my friends, Aline Doherty, Juliana Naveira, and Pedro Henrique Sousa, for their care and support.

I am grateful to Laressa and Maristela for all administrative support, and to Leonardo and Wanderson for all IT support.

I would like to thank the healthcare professionals who took care of my physical and mental health during this process.

Finally, I would like to thank all the teachers I have had throughout my life for their noble profession, which continues to inspire me. You are lights in the lives of your students. Education has the power to transform a person´s reality. Congratulations on your courage to teach!

“A educação é um ato de amor e, por isso, um ato de coragem.”

Paulo Freire

RESUMO

Este estudo avalia a eficácia de atributos sísmicos para identificar estruturas de prováveis impactos soterradas na Bacia de Santos, com foco nas crateras Ilha do Mel (Mioceno-Plioceno) e Praia Grande (Turoniano). Cinco atributos – cubo de coerência, amplitude RMS (root-mean-square), relevo, sweetness e impedância acústica relativa – foram aplicados a volumes sísmicos 3D pós-empilhamento (espaçamento entre inlines de 25 m e crosslines 12,5 m) para realçar feições típicas de cratera de impacto complexas, como falhas normais concêntricas e soerguimento centrais. O cubo de coerência mostrou-se o mais eficaz, delineando claramente padrões de falhas concêntricas e um soerguimento central, enquanto o atributo relevo destacou a expressão das falhas, mas não definiu tão bem a morfologia da cratera. Os atributos amplitude RMS e sweetness evidenciaram intervalos arenosos, auxiliando na interpretação litológica. O mapeamento estrutural dos horizontes interpretados confirmou redes de falhas anulares e soerguimentos centrais, consistentes com a morfologia de crateras complexas. Apesar da ausência de evidências diretas de metamorfismo de choque como por exemplo, cones de estilhaçamento – shatter cones – e feições de deformação planar, as assinaturas sísmicas apoiam fortemente uma origem por impacto. O estudo demonstra que atributos baseados em coerência são ferramentas valiosas para a detecção de crateras de impacto no subsolo.

Palavras-chave: Estruturas de Impacto; Atributos Sísmicos; Bacia de Santos.

ABSTRACT

This study evaluates the effectiveness of seismic attributes for identifying buried impact structures in the Santos Basin, focusing in the Ilha do Mel (Miocene-Pliocene) and Praia Grande (Turonian) craters. Five attributes – coherence cube, root-mean-square (RMS) amplitude, relief, sweetness, and relative acoustic impedance – were applied to 3D post-stack seismic volumes (inline spacing 25 m, cross-line 12,5 m) to enhance features typical of complex impact craters, such as concentric normal faults and central uplifts. The coherence cube proved most effective, clearly delineating concentric fault patterns and a central uplift, while the relief attribute highlighted fault expression but did not define the crater morphology as expected. RMS amplitude and sweetness highlighted sandy intervals, supporting lithological interpretation. Structural mapping of interpreted horizons confirmed annular fault networks and central uplifts consistent with complex crater morphology. Although direct shock-metamorphic evidence (e.g., shatter cones, planar deformation features) is lacking, the seismic signatures strongly support an impact origin, and the study demonstrates that coherence-based attributes are valuable tools for subsurface impact-crater detection.

Keywords: Impact Structures; Seismic Attributes; Santos Basin.

TABLE OF CONTENTS

LIST OF FIGURES……15

1. INTRODUCTION 19

2. IMPACT CRATERS 20

2.1 Morphology of impact craters 20

2.2 Formation of impact structures 22

2.3 The challenge of identifying buried impact structures 24

2.4 Geophysical signatures of impact craters 25

2.5 Relevance of Impact Craters Research 25

2.6 Impact structures in sedimentary basins 27

2.6.1 Ames Crater 27

2.6.2 Chicxulub Crater 28

2.6.3 Nadir Crater 28

2.6.4 Brazilian impact structures 29

3. GEOLOGIC SETTING 31

3.1 Tectono-sedimentary evolution of Santos Basin 32

3.2 Stratigraphy and depositional systems 34

3.2.1 Basement 36

3.2.2 Guaratiba Group 36

3.3 Petroleum system of the Santos Basin 44

3.4 Turbidite systems 45

4. LITERATURE REVIEW 48

4.1 Seismic Reflection Method 48

4.2 Seismic Processing 50

4.2.1 Migration 51

4.3 Seismic Attributes 52

4.3.1 Amplitude Envelope 54
4.3.2 Instantaneous Frequency 55
4.3.3 Sweetness 56
4.3.4 Root-mean-square amplitude 57
4.3.5 Relief 58
4.3.6 Coherence 59
4.3.7 Relative Acoustic Impedance 60
5. DATA AND METHODS 61
5.1 Seismic database 61
5.2 Seismic interpretation and seismic attributes application 62
6. RESULTS 63
6.1 Ilha do Mel Structure 63
6.1.1 Seismic-stratigraphy and structural framework 63
6.1.2 Attribute analysis on mapped horizons 67
6.2 Praia Grande structure 70
7. Discussion 77
7.1 Geometry and structural interpretation 77
8. Conclusions 79
REFERENCES 80

LIST OF FIGURES

Figure 1. Schematic cross sections through simple (a) and complex (b and c) impact structure from Osinski (2006). 21
Figure 2. Photo by the author at the Barringer Crater, Arizona, United States. 22
Figure 3. Schematic model of the impact sequence at the Nadir impact site (Coast of Guinea, West Africa), based on seismic observations and analog models (Nicholson et al., 2022). This figure illustrates the formation of a complex crater, analogous to the Praia Grande and Ilha do Mel structures, which occur in a marine geological setting. It is worth noting that this structure is very likely a meteorite impact crater, although no drilling confirmation is available. 23
Figure 4. Shock features recorded in terrestrial impact structures and their frequency (Kenkmann, 2021). PDF is Planar Deformation Feature. PF is Planar Feature. FF is Feather Feature. Diaplectic quartz glass. Ballen QTZ is ballen quartz. PDF FSP is Planar Deformation Feature in Feldspar. 24
Figure 5. (A) Shatter cones formed in basalt from Vista Alegre, Brazil (Crosta, 2024). (B) planar deformation features from Domo de Vargeão, Brazil (Crosta et al., 2005). 25
Figure 6. Seismic characteristics of the Nadir Crater, offshore West Africa, illustrating features typical of a complex impact structure (Nicholson et al., 2022). 29
Figure 7. Location map of Brazilian impact structures with the two sedimentary basins, Parana (1) and Parnaiba (2), outlined. In the background, is Brazil's geological chart at 1:1 million (CPRM 2004) (Crosta, 2024). 30
Figure 8. Location map showing the two seismic volumes used in this study and the associated impact structures. The Praia Grande structure is located at the northernmost yellow marker, whereas the Ilha do Mel structure is located to the south. The red lines correspond to the seismic data used in this study. 31
Figure 9. Schematic diagram showing sequence of events during the break-up of Gondwana and formation of the passive margin sedimentary basins in the eastern Brazilian margin. Dotted line represents lake and sea-level at different stages of basin evolution (Mohriak et al., 2008). 34

Figure 10. Stratigraphic chart of the Santos Basin (Modified from Moreira et al., 2007). 35
Figure 11. Simplified conceptual model illustrating the general geology and hydrology of the pre-salt rift system (Pietzsch et al., 2018). 38
Figure 12. Simplified stratigraphy and comparison between the pre- and post-salt plays of Santos Basin (Baptista et al. 2023, after Moreira et al. 2007) 45
Figure 13. Schematic subdivision of a turbidity current (head, body, and tail). Modified from D'Ávila et al., 2008. 46
Figure 14. Conceptual diagram showing the main elements of a turbidite depositional system (Modified from Mutti, 1999). 47
Figure 15. Distribution of the main faces and dominant grain size according to the depositional model for high-efficiency turbidite systems (modified from Mutti, 1999 by Morais, 2017, and translated into English in this work). 48
Figure 16. Marine seismic geometry: (a) source-receiver configuration illustrating wavefronts and rays (perpendicular to the wavefronts), with the angle of incidence increasing as offset increases; (b) shot gather representation of recorded energy. In a horizontally layered medium, reflections describe a hyperbolic trajectory on the gather. The reflection amplitude is controlled by the acoustic contrast across layer boundaries and by geometric spreading, which causes amplitude decay with increasing travel distance (Simm & Bacon, 2014). 49
Figure 17. The convolutional model of the reflection seismic trace, showing the trace as the convolved output of reflectivity function with an input pulse, and the relationship of the reflectivity function to the physical properties of the geological layers (Kearey, 2002). 50
Figure 18. (a) Seismogram and (b-f) the migration results of increasing the velocity from 1500 m/s to 2500 m/s at each 250 m/s increment. Equation 2 is used for zero-offset migration (Santos et al. 2020). 51
Figure 19. A time line of seismic attribute developments and their relationship to key advances in seismic exploration technology (after Barnes (2001) as cited in Chopra & Marfurt (2005)). 53
Figure 20. Seismic attributes categorized by property (Barnes, 2016, p.5) 54
Figure 21. Isometric diagram of portion of an actual seismic trace. Amplitude envelope is highlighted in red (after Taner et al., 1979). 55

Figure 22. Real (a) and quadrature (b) traces for a portion of an actual seismic trace. Also shown is the envelope [dotted curve in (a, b)], phase (c), instantaneous frequency (d), and weighted average frequency [dotted curve in d] (Taner et al., 1979). 56
Figure 23. Formula of the Amplitude Volume Technique, where (1) is the RMS average, (2) is the inverse Hilbert Transform with a -90º phase rotation, and (3) is the window size, corresponding to the elementary seismic bed (after Bulhões and de Amorim, 2005).....59
Figure 24. Flowchart of the methodology used in this study.....61
Figure 25. Seismic inline 1246 showing interpreted horizons (H1, H2, and H3) and faults. 63
Figure 26. Interpreted faults on the H1 horizon slice overlain on the coherence cube. 64
Figure 27. Interpreted faults on the H2 horizon slice overlain on the coherence cube. 66
Figure 28. Interpreted faults on the H3 horizon slice overlain on the coherence cube. 67
Figure 29. Composite maps from a horizon slice near the top of the structure designated as H1 horizon slice (A), coherence cube (B), RMS amplitude (C), relief (D), sweetness (E), and relative acoustic impedance (F). 68
Figure 30. Composite maps from a horizon slice near the top of the structure designated as H2 horizon slice (A, seismic section without attributes) and its seismic attributes: coherence cube (B), RMS amplitude (C), relief (D), sweetness (E), and relative acoustic impedance (F).....69
Figure 31. Composite maps from a horizon slice near the top of the structure designated as H3 horizon slice (A, seismic section without attributes) and its seismic attributes: coherence cube (B), RMS amplitude (C), relief (D), sweetness (E), and relative acoustic impedance (F).....70
Figure 32. Seismic Inline 1726 (time) across the Praia Grande impact structure showing the interpreted horizons (Santonian, D1 unconformity, Turonian, Albian, Top of salt, and Base of salt) and the mapped faults. 71
Figure 33. Seismic Inline 1726 (time) processed with Relief seismic attribute, aiming to highlight structural features and stratigraphic discontinuities within Praia Grande impact crater area. 72

Figure 34. Santonian horizon slice in time. The color scale represents two-way travel time (ms), with warmer colors indicating shorter travel times (shallower areas) and cooler colors indicating longer travel times (deeper areas). Red corresponds to approximately 3111 ms, whereas blue corresponds to approximately 4233 ms. 73
Figure 35. 3D view of the Horizon Slice D1 Unconformity processed with a seismic coherence attribute (grayscale) highlighting the structural expression of the impact crater. (A) Uninterpreted surface displaying a highly chaotic central core corresponding to the central uplift, surrounded by distinct concentric black lineaments that mark physical discontinuities and fault scarps. (B) Interpreted structural framework displaying 3D fault planes (colored blades in red, magenta, light blue, and green) tracking the concentric lineaments, illustrating the listric normal ring fault systems developed during the crater modification stage. Note the 5 km scale bar for regional dimensioning. 74
Figure 36. Turonian horizon slice. The color scale represents two-way travel time (ms), with warmer colors indicating shorter travel time (shallower areas) and cooler colors indicating longer travel times (deeper areas). Red corresponds to approximately 3566 ms, whereas blue corresponds to approximately 4755 ms. 75
Figure 37. Turonian horizon slice displayed with the coherence cube attribute. Darker colors indicate lower coherence values. 76
Figure 38. Albian horizon slice. The color scale is in two-way travel time (ms), with red representing shallower areas (~3700 ms) and blue representing deeper areas (~4827 ms). 76

1. INTRODUCTION

Impact cratering is a relevant geological process that has shaped planetary surfaces throughout Solar System history (Kelly & Dahille, 1953; French, 1998). The study of impact structures is fundamental to understanding the origin, extinction and evolution of life on Earth (French, 1998), as well as to the exploration of mineral and petroleum resources associated with these structures (Mazur et al., 2000; Zucolotto et al., 2013; Kenkmann, 2021). However, due to erosion, sediment transport, sedimentation and tectonic deformation processes, the preservation of terrestrial impact craters is significantly compromised when compared to other planetary bodies. Consequently, geophysical methods play a crucial role in the identification of buried impact craters.

Numerous geophysical studies have addressed the identification and characterization of impact structures (e.g., Pilkington and Grieve, 1992; Correia et al. 2005; Glikson & Uysal, 2013; Gulik et al., 2013; Pereira et al., 2024; Armour et al., 2024; Avona et al., 2025; Nicholson et al., 2022). According to Kenkmann (2021), 208 terrestrial impact structures have been identified worldwide, nine of which have been confirmed in Brazil (Crosta, 2024). Reflection seismic methods, both onshore and offshore, are among the most powerful tools for imaging and analyzing the concealed subsurface geometry of impact craters (Kenkmann, 2021).

The Santos Basin, a prolific offshore petroleum province off southeastern Brazil, host two candidate structures that exhibit several hallmarks of complex impact craters: the Ilha do Mel (Miocene-Pliocene) and Praia Grande (Turonian). These structures were previously investigated by Menezes et al. (2012) and Correia et al. (2005), respectively, yet a systematic seismic-attribute technique for their discrimination has not been undertaken. Therefore, the main objective of this thesis embraces the evaluation effectiveness of seismic attributes on the characterization of impact structures. To this end, seismic data from these Brazilian impact structures were analyzed. The present thesis introduces a comprehensive workflow that integrates five distinct seismic attributes - coherence cube, root-mean-square (RMS) amplitude, relief, sweetness and relative acoustic impedance – applied to high-resolution 3D post-stack volumes. By juxtaposing the attribute responses across multiple interpreted horizons,

the study quantifies each attribute's capacity to accentuate structural and lithological signatures of impact-related deformation. The coherence cube, in particular, demonstrates the highest efficacy in delineating concentric normal-fault systems and the central uplift, thereby providing the clearest subsurface expression of a complex crater in the basin to date. Furthermore, this study contributes to the chronological framework of the region by constraining the age of the Praia Grande structure to the Turonian rather than the Santonian, as suggested in previous literature. Chapter 2 provides an overview of impact crater morphology, formation processes, diagnostic elements, and the scientific relevance of studying impact craters. Chapter 3 describes the geologic setting of the Santos Basin. Chapter 4 presents a literature review of seismic reflection methods and seismic attributes. Chapter 5 presents the methodology. Chapter 6 presents the results, and Chapter 7 discusses the findings. Chapter 8 summarizes the conclusions.

2. IMPACT CRATERS

2.1 Morphology of impact craters

Depending on their diameter, terrestrial impact craters are classified into two main types: simple and complex (Figure 1). Simple craters typically have diameters smaller than 4 km in massive crystalline rocks and less than 2 km in sedimentary target rocks (Dence, 1972, cited in Pilkington & Grieve, 1992; French, 1998). In contrast, complex craters have diameters greater than 4 km and are characterized by the presence of a central uplift rather than a simple bowl-shaped depression.

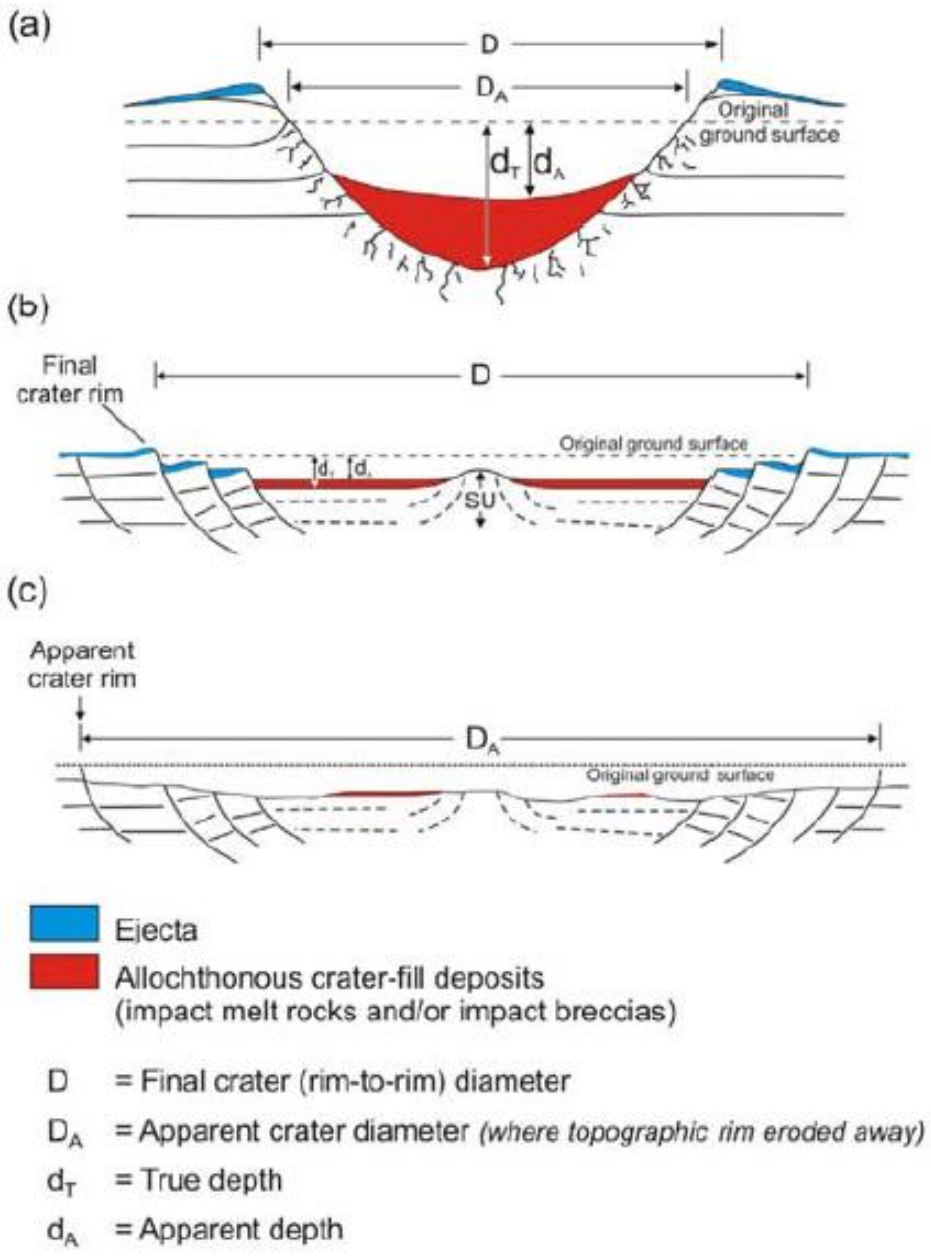


Figure 1. Schematic cross sections through simple (a) and complex (b and c) impact structure from Osinski (2006).

A famous example of a simple crater is the Barringer Crater in Arizona, United States, which is 1.2 km in diameter. The Barringer Crater is approximately 50000 years old. Because it is geologically very young and located in an arid desert region, it has undergone very little erosion over the millennia, making it the best-preserved impact crater on our planet.



Figure 2. Photo by the author at the Barringer Crater, Arizona, United States, 2024.

2.2 Formation of impact structures

French (1998, pp.18-23) and Osinski (2006) divided the formation of impact structures into three main stages: contact and compression, excavation, and modification. The first stage begins when the projectile contacts the surface, transferring its kinetic energy into the soil and rocks through shock waves (Figure 3). At the point of impact, pressures can exceed 100 GPa, causing complete melting or even vaporization of the projectile within a few seconds (French, 1998). At greater distances from the impact point, the peak shock-wave pressure decreases and propagates as regular elastic and seismic waves. Due to these relatively lowering pressures, these waves generally do not produce permanent deformation of the rocks through which they pass. However, seismic waves can induce fracturing, brecciation faulting, and near the surface, landslides and tsunamis.

The excavation stage (Figure 3B) begins immediately after the compression stage, during which shock wave energy is converted into kinetic energy (Vasconcelos, 2007). Target rocks are ejected outward from the impact point, generating a symmetrical excavation flow around the affected center. The vertical movement of material creates

a transient cavity, which is a roughly spherical depression with a raised rim, typically about one-third of its diameter in depth. Depending on the water depth, impact penetrating depth and rock substrate, a phenomenon of rock fusion may occur generating a complex substrate of high resolution.

Shortly after the transient crater reaches its maximum size, the modification stage begins (Figure 3C and 3D). The central uplift may form before the maximum crater diameter is fully achieved, occurring in the transitional interval between the excavation and modification stages. During the modification stage, the transient crater undergoes immediate adjustments due to gravitational forces and rock mechanics, including the formation of collapse faults along the crater walls.

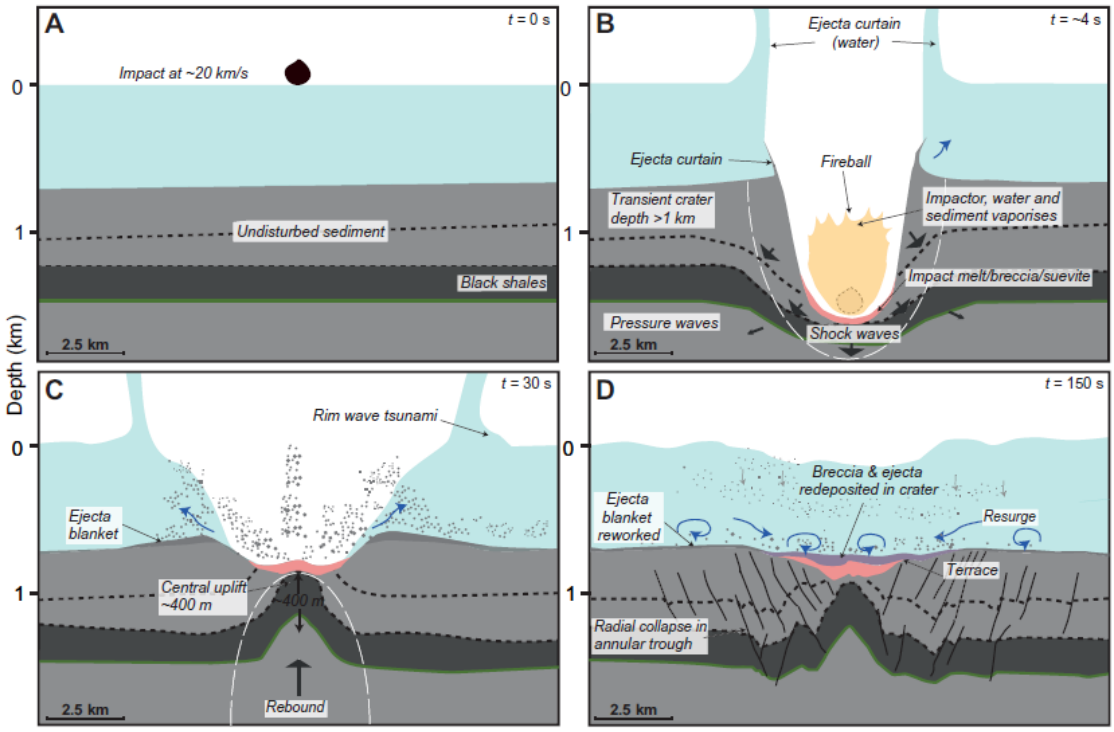


Figure 3. Schematic model of the impact sequence at the Nadir impact site (Coast of Guinea, West Africa), based on seismic observations and analog models (Nicholson et al., 2022). This figure illustrates the formation of a complex crater, analogous to the Praia Grande and Ilha do Mel structures, which occur in a marine geological setting. It is worth noting that this structure is very likely a meteorite impact crater, although no drilling confirmation is available.

2.3 The challenge of identifying buried impact structures

Erosion rapidly removes the original morphological features of terrestrial impact craters and, over time, erases much of their geological and structural signatures (Pilkington & Grieve, 1992). In the case of submerged craters, chemical weathering further modifies the target rocks. Additionally, burial and tectonics processes complicate the identification of impact structures. The most direct and definitive evidence for confirming an impact origin comes from shock metamorphism (Figure 4), such as shatter cones, planar deformations features in quartz, and high-pressure minerals including coesite and stishovite (French, 1998; Zucolotto et al., 2013; Kenkmann, 2021). However, drilling to obtain such evidence is very expensive, which underscores the importance of applying geophysical methods for crater identification.

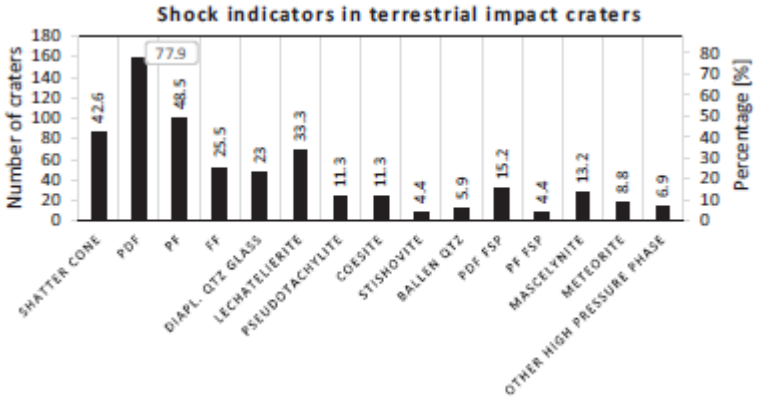


Figure 4. Shock features recorded in terrestrial impact structures and their frequency (Kenkmann, 2021). PDF is Planar Deformation Feature. PF is Planar Feature. FF is Feather Feature. Diaplectic quartz glass. Ballen QTZ is ballen quartz. PDF FSP is Planar Deformation Feature in Feldspar.

Figure 5 shows an example of shatter cones and planar deformation features in quartz.

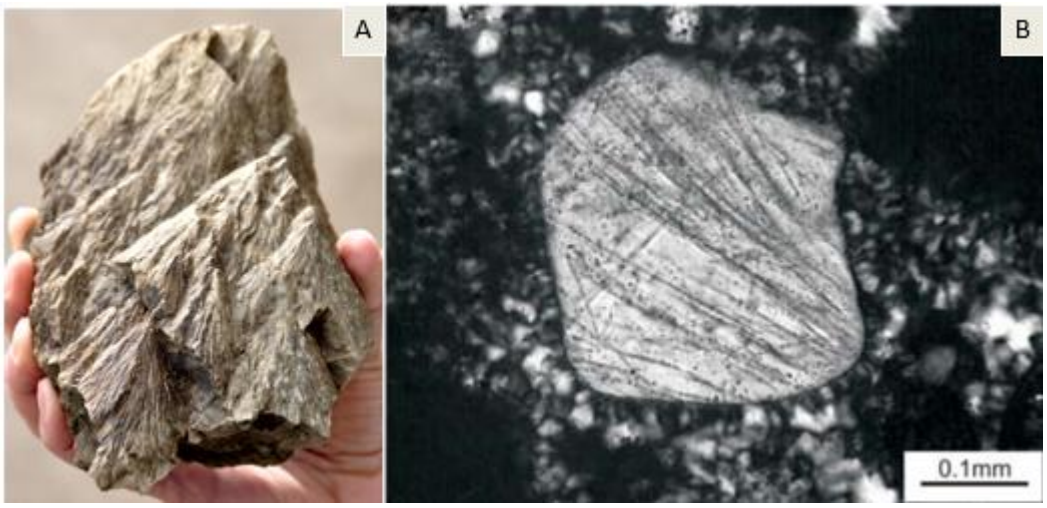


Figure 5. (A) Shatter cones formed in basalt from Vista Alegre, Brazil (Crosta, 2024). (B) planar deformation features from Domo de Vargeão, Brazil (Crosta et al., 2005).

2.4 Geophysical signatures of impact craters

Seismic data permit visualize the morphology of complex impact craters, including rim faults, central uplifts, chaotic infill, annular moats, and uplifted of deep reflectors (e.g., Glikson & Uysal, 2013; Gulik et al., 2013; Nicholson et al., 2022, 2025). Incoherent reflections and reduced seismic velocities are commonly observed due to brecciation and fracturing, with reflection coherence generally increasing away from and beneath the center of the structure (Pilkington e Grieve, 1992).

Impact craters typically exhibit a negative gravity anomaly (Pilkington & Grieve, 1992). For instance, bouguer gravity data over the Chicxulub crater revealed an approximately 180 km diameter circular negative anomaly of 30 mgal, consistent with the signature of other large impact craters (Hildebrand et al., 1991). Complex magnetic anomalies are also frequently observed, reflecting lithological variations within and surrounding the crater.

2.5 Relevance of Impact Craters Research

The scientific significance of impact craters lies on the fact that meteorite impacts were a primary process during the early stages of the Solar System’s formation

and evolution, affecting all planetary bodies, including Earth (Crosta, 2024). Furthermore, meteorite impacts are closely linked to related to the evolution and extinction of life on Earth. It is widely accepted that impacts played a fundamental role in providing the conditions and thermal energy necessary for the transition from prebiotic chemistry to the emergence of the first life forms on Earth (Crosta, 2024). In addition, one of Earth's five major mass extinctions, the Cretaceous-Paleogene boundary event, which occurred approximately 65,5 million years ago, was caused by the impact of an asteroid on the Yucatan carbonate platform in Chicxulub. Geophysical models indicate that the large quantities of water, dust, and climate-forcing gases released by this impact would dramatically alter the climate system, generating mass flows, and megatsunamis in the Gulf of Mexico and surrounding areas (Alvarez et al., 1980; Hildebrand et al., 1991; Toon et al., 1997; Pierazzo et al., 2003; Schulte et al., 2010). According to Scotese et al. (2021), "temperatures can fall rapidly, creating short-lived icehouse worlds, due to major bolide impact events (e.g., K/T boundary impact Winter or possibly the Hirnantian Ice Age). Very large impact events (crater size > 150 km) may also trigger large igneous eruptions that create a period of global warming that follows impact-related cooling (e.g., Chicxulub impact event)".

The economic significance of impact craters stems from the fact that approximately 25% of all known craters have potential economic value (Mazur et al., 2000). Natural resources associated with impact structures can be classified into three types: progenetic, syngenetic, and epigenetic (Zucolotto et al., 2013; Grieve, 2005; Kenkmann, 2021). Progenetic resources are pre-existing deposits in the target region that may become more accessible as a direct result of the impact. Syngenetic resources are formed directly by the impact process itself. Epigenetic resources are generated by post-impact processes, such as hydrothermal activity, often involving fluid flow and hydrocarbon migration.

Examples include the gold and uranium deposits in the Vredefort crater of the Witwatersrand Basin in South Africa, and the uranium deposit in Carswell, Canada, which are progenetic (Zucolotto et al., 2013; Kenkmann, 2021). Syngenetic diamond deposits occur in Russia, including Popigai, Puchezh-Katunki, and Kara. Epigenetic mineralization is observed in the Sudbury structure in Canada (Zucolotto et al., 2013). Furthermore, providing a prime example of impact-induced hydrocarbon accumulation, the breccias generated by the Chicxulub event on the Gulf of Mexico carbonate

platform did more than just shape the regional geology; they constituted the reservoir rocks for Mexico's most prolific oil fields, including Cantarell and the Ku-Maloob-Zaap (KMZ) complex (Alvarez et al., 1980; Grajales-Nishimura et al., 2000; Texeira et al., 2014).The Ames Crater in the United States is another example where impact-induced fracturing created highly permeable reservoirs (Carpenter et al., 1997).

2.6 Impact structures in sedimentary basins

The table below presents the diameter and age of selected international and national impact craters.

Table 1. Diameter and age of selected impact craters. Adapted from Zucolotto et al. (2013) and Crosta (2024), including the age of Praia Grande determined in this study.

IMPACT CRATER	LOCALITY	DIAMETER (km)	AGE (Ma)	CRATER STATUS
Vredefort	South Africa	300	1970±100	Confirmed
Sudbury	Ontario, Canada	250	1850±3	Confirmed
Chicxulub	Yucatan, Mexico	180	65.5	Confirmed
Manicouagan	Quebec, Canada	100	212±1	Confirmed
Popigai	Russia	100	35±5	Confirmed
Acraman	Southern Australia	90	570	Confirmed
Chesapeake Bay	United States	90	35±0.6	Confirmed
Mjølnir	Barents Sea	40	143±20	Confirmed
Ames	United States	16	470	Confirmed
Nadir	West Africa	8.5	66	Confirmed despite the lack of evidence for shock metamorphism
Araguainha Dome	Brazil	40	254.7±2.5	Confirmed
Vista Alegre	Brazil	9.5	<132	Confirmed
Vargeao Dome	Brazil	12.4	<132	Confirmed
Cerro do Jarau	Brazil	13.5	<132	Confirmed
Serra da Cangalha	Brazil	13.7	<200	Confirmed
Riachao	Brazil	4.5	<200	Confirmed
Nova Colinas	Brazil	6.5-7.0	<200	Confirmed
Sao Miguel do Tapuio	Brazil	20	<150	Confirmed
Santa Marta	Brazil	10	<100	Confirmed
Praia Grande	Brazil	20	94-90	In study
Ilha do Mel	Brazil	6	5	In study
Colonia	Brazil	3.5	36-5	In study

2.6.1 Ames Crater

The Ames Crater is located within Anadarko Basin, Oklahoma, United States and represents an example of hydrocarbon accumulation associated with impact-induced fracturing. It dates back to the Ordovician. The impact penetrated the sedimentary sequence and reached the crystalline basement. The fractures generated by the impact created highly permeable reservoirs. Hydrocarbons migrated from

source rocks within the Anadarko Basin into these fractured zones. For instance, the Arbuckle Dolomite normally does not exhibit significant matrix porosity or permeability, and reservoir size and quality are typically limited (Carpenter & Carlson, 1997). However, in April 1991, excellent flow rates for both gas and oil were observed during separate tests. According to Carpenter & Carlson (1997), the Upper Arbuckle produced gas at a rate of 3,440 MCFGPD (million cubic feet of gas per day), demonstrating how impact-induced fracturing can significantly enhance reservoir performance.

2.6.2 Chicxulub Crater

The Chicxulub Crater has an approximate diameter of 180 km standing as the largest impact craters on Earth. It is located on the Yucatan Peninsula in Mexico. Its formation dates to about 65,5 Ma and is associated with the major mass extinction at the Cretaceous-Paleogene extinction event (Alvarez et al., 1980; Hildebrand et al., 1991; Schulte et al., 2010; Gulick et al., 2013). This impact had major consequences, such as giant tsunamis, the release of dust and gases into the atmosphere that blocked sunlight, and extreme climate changes that collapse food chains (Schulte et al., 2010).

2.6.3 Nadir Crater

The Nadir Crater is located on the Guinea Plateau, West Africa, and has a diameter of 8.5 km. Its stratigraphic framework suggests that the crater formed at or near the Cretaceous-Paleogene boundary, approximately the same age as the Chicxulub impact crater (Nicholson et al. 2022). Figure 6 shows the Nadir complex crater, where the central uplift is observed.

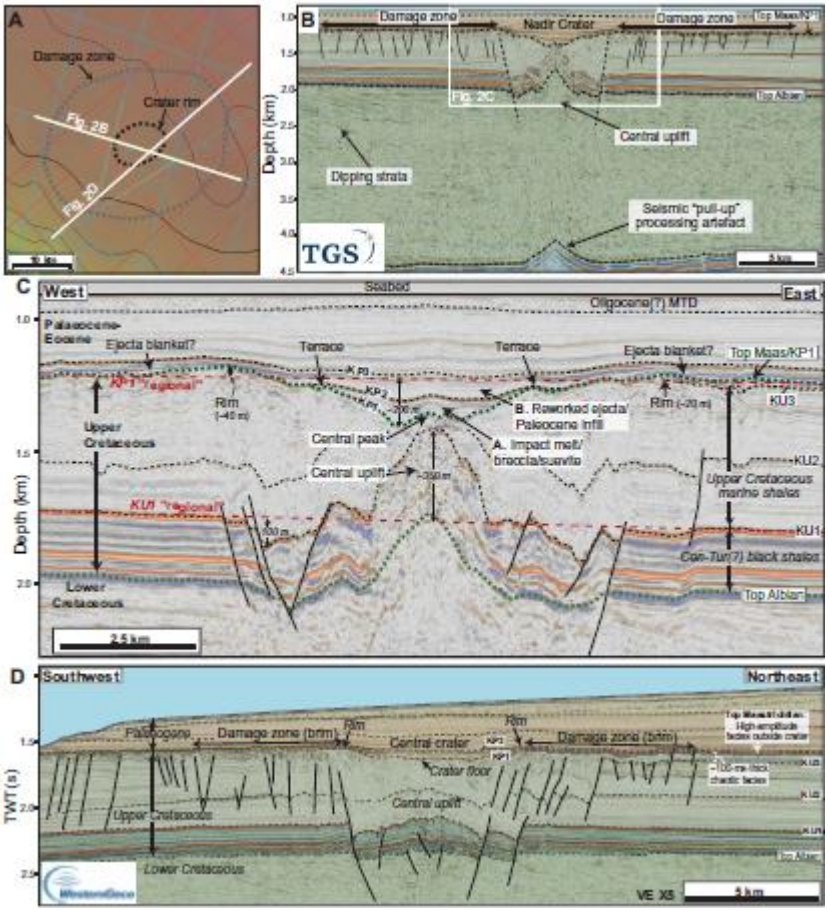


Figure 6. Seismic characteristics of the Nadir Crater, offshore West Africa, illustrating features typical of a complex impact structure (Nicholson et al., 2022).

2.6.4 Brazilian impact structures

In Brazil, there are no confirmed records of economically productive petroleum systems directly associated with impact craters. There are nine confirmed impact craters in Brazil, while three others remain unconfirmed, including Praia Grande, Ilha do Mel, and Colonia (Figure 7).

The Araguainha impact structure (254,7 $\pm$ 2.5 Ma) includes a prominent central uplift represented by the Araguainha Dome. Although this structure is not the main focus of this study, it is important to briefly discuss it because it represents the largest known impact structure in South America (40 km) and one of the largest in the world. Moreover, it displays one of the most diverse assemblages of geological features associated with impact cratering (shatter cones, planar deformation features, planar

fractures and feather features, among others) and it's the best characterized structure of this type in Brazil from geological, structural, geochemical, and geophysical perspectives (Crosta, 2024).

In addition to containing diagnostic elements of an impact crater, the structure also preserves extensive soft-sediment deformation features (seismites) and tsunami-related deposits (tsunamites). According to Tohver et al. (2018), these seismites are widespread at distances of approximately 50-1000 km from the impact site. The large spatial extent of these deposits highlights the enormous energy released during a meteorite impact.

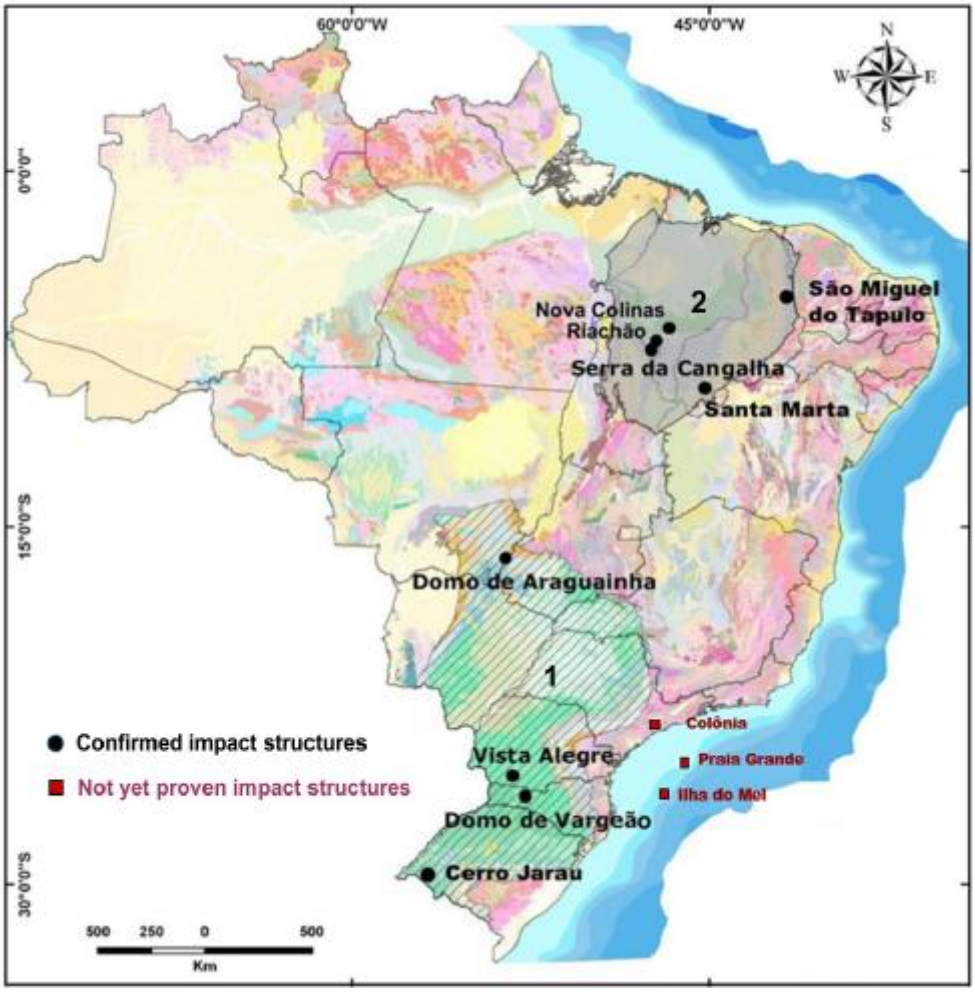


Figure 7. Location map of Brazilian impact structures with the two sedimentary basins, Parana (1) and Parnaiba (2), outlined. In the background, is Brazil's geological chart at 1:1 million (CPRM 2004) (Crosta, 2024).

3. GEOLOGIC SETTING

The two referred impact structures investigated in this study are located within the Santos Basin (Figure 8). The Santos Basin is a passive-margin basin situated in southeastern Brazil, extending along the coasts of the states of Rio de Janeiro, Sao Paulo, Parana and Santa Catarina. The basin covers an area of approximately 352000 km^2 and is bounded to the north by the Cabo Frio High and the Campos Basin and to the south by the Florianopolis Fracture Zone and the Pelotas Basin (Moreira et al. 2007; Siqueira et al., 2024).

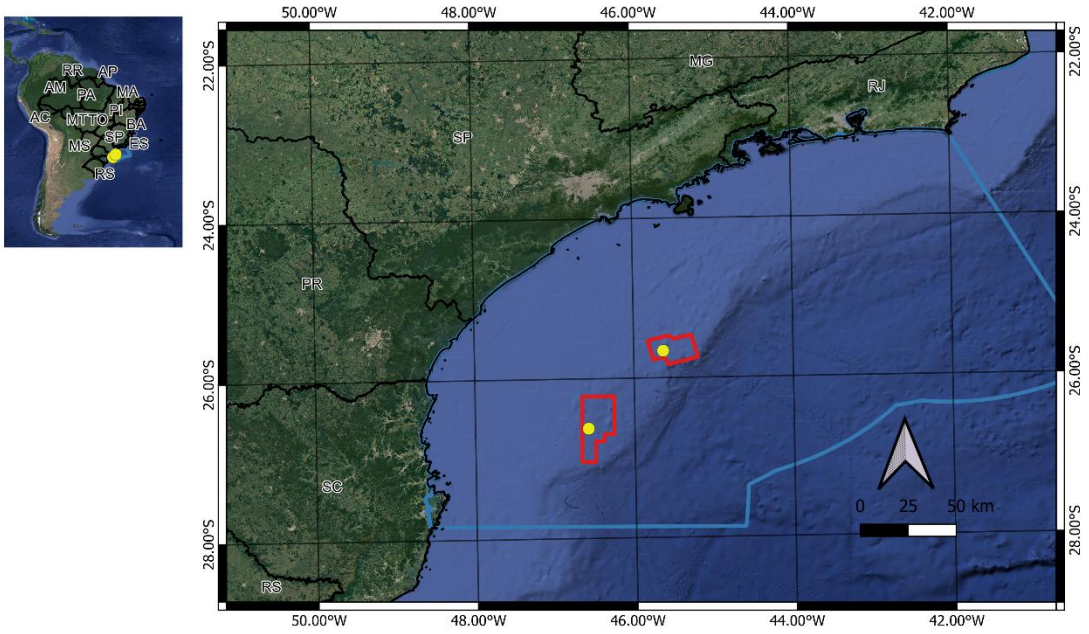


Figure 8. Location map showing the two seismic volumes used in this study and the associated impact structures. The Praia Grande structure is located at the northernmost yellow marker, whereas the Ilha do Mel structure is located to the south. The red lines correspond to the seismic data used in this study.

The discussed Praia Grande impact structure is located approximately 200 km offshore from the city of Praia Grande, southeastern Brazil, at coordinates 25°38’50”S

and 45°37’30”W (Correia et al., 2005). The structure is buried beneath undisturbed sedimentary rocks at a depth of approximately 4 km, dating back to the Santonian (Correia et al. 2005). However, it is interpreted in this study as the result of meteorite impact that occurred during the Turonian. In contrast, the Ilha do Mel impact structure is located about 210 km offshore from the coast of the state of Parana, at coordinates 26°37’48.29”S and 46°36’0.37”W. This structure is assigned to the Miocene-Pliocene and is buried beneath approximately 400 m of post-impact sediment (Menezes et al., 2012).

3.1 Tectono-sedimentary evolution of Santos Basin

The tectono-stratigraphic evolution of the Santos Basin is closely linked to the rifting of the Gondwana supercontinent, culminating with the opening of the South Atlantic Ocean during Early Cretaceous (Moreira et al., 2007; Mohriak et al., 2008). According to Cainelli & Mohriak (1999), the geodynamic evolution of the sedimentary basins along the eastern Brazilian margin, within the Santos Basin characterized by five tectonic phases (Figure 9). Nevertheless, Moreira et al. (2007) divided tectonic evolution in three stages: rift, post-rift, and drift (Figure 10). Next, the five phases reported by Mohriak et al. (2008) will be correlated with the work of Moreira et al. (2007).

The first phase (Figure 9-I) marks the onset of the extensional process that led to the separation of South America and Africa during the Late Jurassic-Early Cretaceous. During this stage, thinning of the crust and lithospheric mantle occurred, accompanied by minor asthenospheric uplift, leading to the development of upper-crustal faults associated with depocenters characterized by relatively thin rift-related sedimentation.

The second phase (Figure 9-II) is characterized by the increase of lithospheric stretching and asthenospheric uplift (McKenzie 1978; White & McKenzie 1988), during Early Cretaceous-Barremian (syn-rift I and syn-rift II, corresponding to the rift stage of Figure 10). This event represents the principal phase of intracontinental rifting in this sector of the South Atlantic and was accompanied by the eruption of Late Jurassic-

Early Cretaceous tholeiitic basalts, both onshore and along the nascent continental margins (Mohriak et al., 2008). The higher incidence of faulting results in the formation of half-grabens filled with continental sediments of lacustrine origin (Viana, 2018).

The third phase (Figure 9-III) marks the termination of syn-rift extension and is characterized by a progressive decline in the activity of major faults that previously rotated rift blocks and their sedimentary cover during the Barremian-Aptian (syn-rift II-sag phases; corresponding to the rift to post-rift stages of Figure 10). Locally, this stage is associated with volcanism, reactivation of large faults, and erosion of rift blocks, culminating in the development of a regional unconformity that smooths the topography. This surface is commonly referred to as the Break-up Unconformity (Falvey, 1974). The unconformity separates continental lacustrine deposits from overlying transitional to marine sediments (Mohriak et al., 2008). Above this unconformity but below the evaporite transitional sequence some sedimentary basins contain a substantial thickness of Aptian siliciclastic and carbonates rocks, interpreted as sag basin fill (Henry & Brumbaugh, 1995)

The fourth phase (Figure 9-IV) is marked by the establishment of a Mid-Atlantic-type ridge system and the onset of concentrated seafloor spreading (Chang et al. 1992; Harry & Sawyer, 1992), from the Aptian to Albian, corresponding to the post-rift stage of Figure 10. The timing of ridge formations can be constrained by the Seaward Dipping Reflectors (SDRs), which overlie the outermost rift blocks of the Santos Basin and Campos basins (Souza et al. 1993; Gladezenko et al. 1997).

The fifth phase (Figure 9-V) spans from the Aptian to the present day and corresponds to the drift stage (Figure 10), being characterized by a progressive increase in bathymetry. This evolution led to a marked deepening of the depositional environment by the Late Albian and to the cessation of shallow-water carbonate deposition by the Cenomanian (Mohriak et al. 2008).

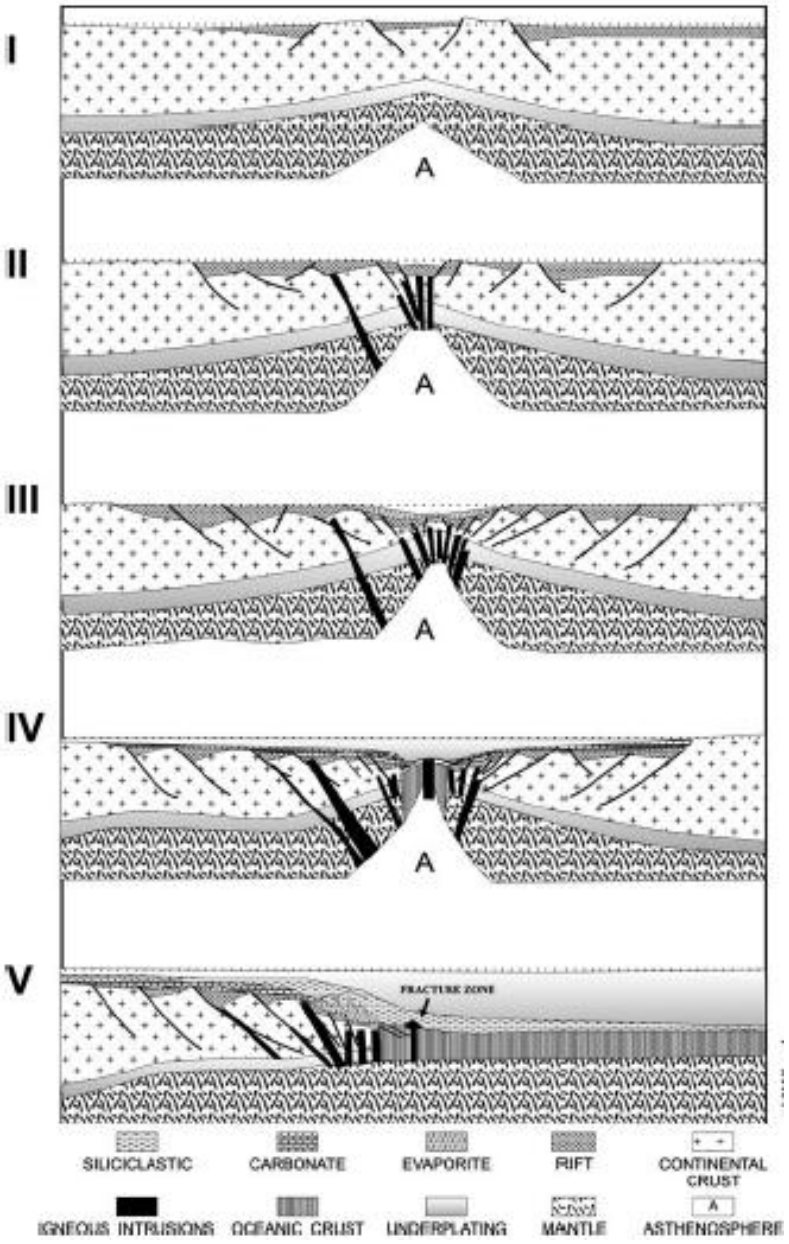


Figure 9. Schematic diagram showing sequence of events during the break-up of Gondwana and formation of the passive margin sedimentary basins in the eastern Brazilian margin. Dotted line represents lake and sea-level at different stages of basin evolution (Mohriak et al., 2008).

3.2 Stratigraphy and depositional systems

Moreira et al. (2007) subdivided the chronolithostratigraphic framework into four major units – Guaratiba, Camburi, Frade, and Itamambuca groups - whose sedimentary infill is closely associated with the rift, post-rift, and drift phases of the evolution of the eastern Brazilian margin (Figure 10). The Praia Grande impact

structure belongs to the Frade Group, whereas Ilha do Mel belongs to the Itamambuca Group. Therefore, both impact structures investigated are located within post-salt sediments of the drift phase (phase V of Figure 9).

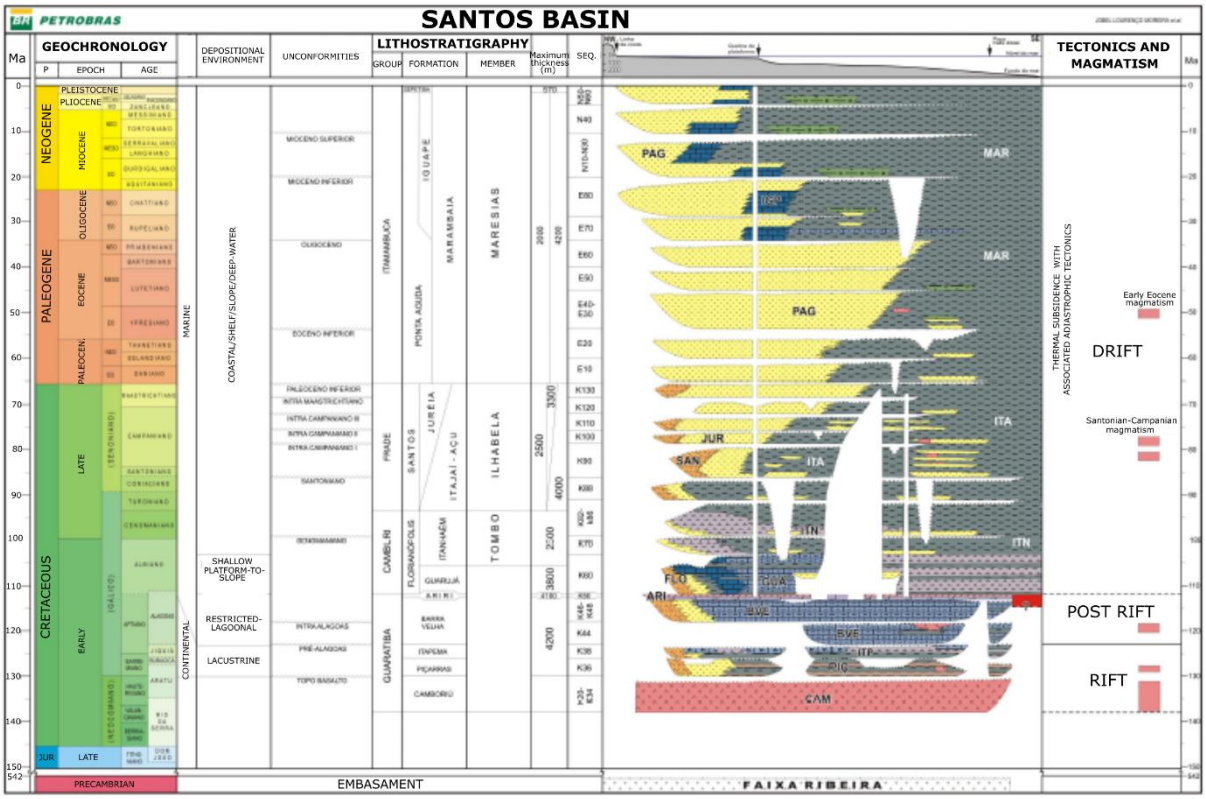


Figure 10. Stratigraphic chart of the Santos Basin (Modified from Moreira et al., 2007).

Both Chang et al. (2008) and Mohriak et al. (2008) are based on the stratigraphic chart of Pereira and Feijo (1994) and they do not mention the work of Moreira et al. (2007). Chang et al. (2008) divided tectonic evolution in three phases: rift (syn-rift I and syn-rift II), sag (syn-rift III), and passive margin. Accordingly, the syn-rift I and syn-rift II phases of Chang et al. (2008) can be correlated with the rift phase of Moreira et al. (2007), the syn-rift III (sag) phase with the post-rift stage, and the passive margin stage with the drift phase.

The study by Chang et al. (2008) was published after that of the Moreira et al. (2007), entitled, "*Interpretation and Mapping of the Petroleum Systems of the Santos Basin*", was developed in 2003 through a partnership between Universidade Estadual

Paulista (UNESP) and the Agencia Nacional do Petroleo, Gas Natural e Biocombustíveis (ANP) (ANP/LEBAC, 2003 cited in Castro, 2019).

3.2.1 Basement

The crystalline basement of the Santos Basin outcropping in the Sao Paulo region is characterized by Precambrian granites and gneisses belonging to the Coastal Complex, as well as metasediments of the Ribeira Belt (Moreira et al., 2007).

3.2.2 Guaratiba Group

The Guaratiba Group is composed of the Camboriu, Picarras, Itapema, Barra Velha, and Ariri Formations. This Group represents the Formations deposited during the rift and transitional phases, prior to the drift phase.

The economic basement of the Santos Basin is defined by the basalts of the Camboriu Formation, which unconformably overlie the Precambrian basement, constituting the K20-K34 Sequence. This corresponds to Phases I and II configurations (pre-rift and syn-rift siliciclastics and volcanics deposits) of Moriahk et al. (2008) (Figure 9), to the phase rift of Moreira et al. (2007) (Figure 10), and phase rift of Chang et al. (2008). Therefore, a volcanic depositional environment.

The K36 Sequence corresponds lithostratigraphically to the Picarras Formation (~130-126,4 Ma), overlies the 130 Ma unconformity (top of basalt) and was divided by Moreira et al. (2007) into proximal and lacustrine portions. The proximal portion is composed of alluvial fans of conglomerates and polymitic sanstones, consisting of basalt and feldspar fragments. The lacustrine portion, in contrast, is composed of sandstones, siltstones, and shales with a stevensitic-talc composition. This corresponds to Phase II configuration (syn-rift I siliciclastics deposits) of Moriahk et al. (2008) (Figure 9), to the phase rift of Moreira et al. (2007) (Figure 10), and phase rift (syn-rift I) of Chang et al. (2008). Therefore, it represents a fluvial-lacustrine depositional environment.

The Itapema Formation (K38) is bounded below by the intra-Barremian unconformity at 126,4Ma and above by the Base Alagoas unconformity (in the Campos Basin referred to as the pre-Alagoas unconformity – DPA). It is recognized by the presence of interbedded grainstones and packstones, bivalve rudstones (coquinas), and dark organich-rich shales in distal portions, as well as alluvial fans composed of conglomerates and sandstones in the proximal facies (Moreira et al., 2007; Carlotto et al., 2017). This corresponds to Phase II configuration (syn-rift II siliciclastics deposits) of Moriahk et al. (2008) (Figure 9), to the phase rift of Moreira et al. (2007) (Figure 10), and phase rift (syn-rift II) of Chang et al. (2008). Therefore, it represents a fluvial-lacustrine depositional environment.

The Barra Velha Formation, deposited during the Aptian, overlies the sediments of the Itapema Formation (K38) and is overlain by the Ariri Formation (K50). It can be subdivided, based on the Intra-Alagoas Unconformity (DIA, 117Ma), which corresponds to a seismic reflector characterized by a strong positive acoustic impedance with regional extent, into a lower interval (Sequence K44) composed of upper rift carbonates, and an upper interval (Sequences K46-K48) that constitutes the carbonates of sag phase (Wright & Barnett, 2015; Buckley et al. 2015).

The carbonates of Barra Velha Formation represent the main reservoir of the pre-salt in the Santos Basin (Szatmari & Milani, 2016). Consequently, considerable emphasis has been given to it in the literature. There are numerous challenging and still uncertain aspects of its evolution, such as its depositional environment, microbial influence on the formation of its rocks, and facies types. As this is not the focus of the present study, the reader is referred to Castro's dissertation (2019, pp 24-43), in which these aspects are thoroughly summarized.

For instance, according to Moreira et al. (2007), the depositional environment of both sequences (K44 and K46-48) of Barra Velha Formation is transitional, between continental and shallow marine settings, and characterized by highly stressful conditions to the phase post-rift. This Formation corresponds to the sag (syn-rift III) of Chang et al. (2008), represented as a restricted marine environment. According to Pietzsch et al. (2018), Gomes et al. (2009) also suggest a traditional environment under marine influence; however, Wright & Barnett (2015) discard this hypothesis of marine origin. Based on sedimentological and mineralogical descriptions, they favor

deposition in alkaline lacustrine environment. Figure 11B illustrates this environment as a shallow, endorheic lake with extensive areal coverage. In addition, according to Szatmari & Milani (2016), the carbonates of the Barra Velha Formation represent the largest non-marine carbonate reservoirs in the world (reaching more than 500 m in thickness), deposited in highly alkaline shallow lacustrine environments.

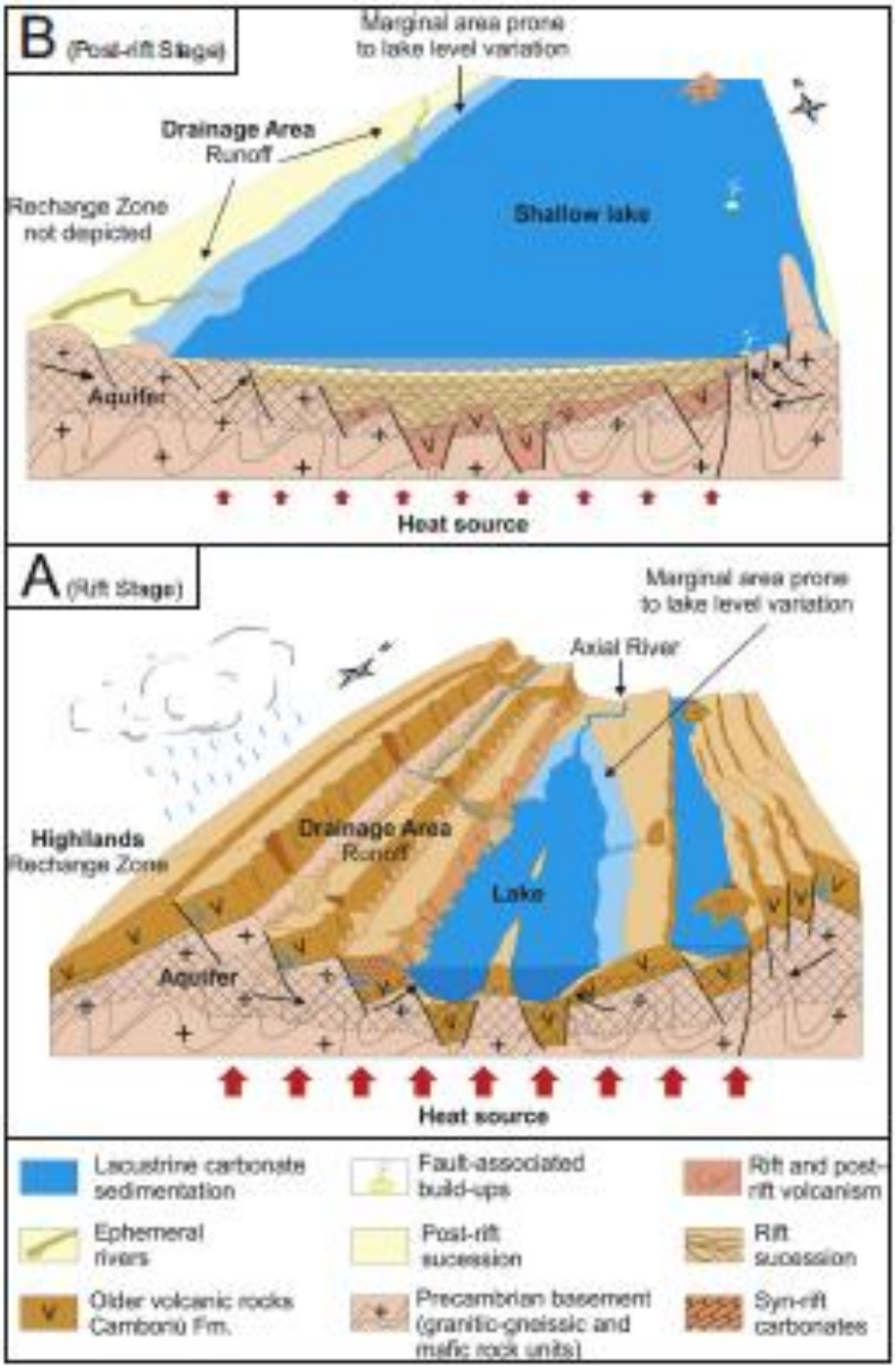


Figure 11. Simplified conceptual model illustrating the general geology and hydrology of the pre-salt rift system (Pietzsch et al., 2018).

The Ariri Formation (K50) is characterized by evaporites that were deposited during the Neoaptian. These evaporites are generally composed of halite and anhydrite. However, the presence of more soluble salts has been identified, such as tachyhydrite, carnallite, and, locally, sylvinite (Moreira et al., 2007). It corresponds to the post-rift phase of Moreira et al. (2007) and to the sag phase (syn-rift III), characterized by a restricted marine depositional environment (Chang et al., 2008).

3.2.3 Camburi Group

The Camburi Group is composed of the Florianopolis, Guaruja, Itanhaem and Tombo Member. The tectonic phase corresponding to this group is the drift phase (Figure 10). This group represents a transgressive phase that culminated in the deposition of the anoxic shales of the Turonian transgression. It encompasses all sediments deposited from alluvial fan systems to bathyal pelites and sandstones, spanning from after the Ariri Formation (K50) to the top of the Cenomanian (Moreira et al., 2007). Thus, they are part of the post-salt deposits.

The Florianopolis Formation comprises the stratigraphic sequences K60, K70, and part of the proximal portion of K82-K86, where sandy and pelitic deposits occur. This Formation corresponds to the proximal facies of Sequence K60 and is composed of conglomerates, sandstones, and shales associated with alluvial fan and deltaic systems.

The Guaruja Formation was deposited in a carbonate platform environment throughout the Albian and is part of Sequence K60. Moreira et al. (2007) physiographically divide it into inner and outer platform environments. In the inner platform, shales and calcilutites of a lagoonal system are found, along with oolitc and/or calcirudites and calcarenites belonging to the shallow bank. In the outer platform, calciludites and marls gradually grade into or interdigitate with dark shales in the basinward portions.

The Itanhaem Formation comprises the stratigraphic sequences K60, K70, and K82-K86. Its lower part is composed of the radioactive Marco Beta shale and the overlying calcilutites of the K60 stratigraphic sequence. In K70, it is interbedded with sandy deposits from systems generated by dense gravitational flows that make up the Tombo Member, corresponding to a relative sea-level rise.

The deposits of Sequences K82-K86 (Florianopolis, Santos, Jureia, Itanhaem Formations, Tombo Member, and Itajai-Acu Formation) record the highest marine transgression in the sedimentary record (Turonian anoxic event). The Itanhaem Formation is characterized by fine-grained sediments (claystones and shales) with higher carbonate content in its basal section. Corresponding to the marls of the palynological interval (Cenomanian unconformity), it was deposited in an upper bathyal environment with episodic anoxic conditions, represented by laminated dark shales. Therefore, these deposits mark a period of marine transgression that culminated in the drowning of the Albian carbonate platform and are succeeded by the Itajai-Acu Formation.

The Tombo Member is composed of sandstones generally confined to depositional lows generated and controlled by Albian salt tectonics. In addition, the Tombo Member comprises the stratigraphic sequences K70 and K82-K86.

3.2.4 Frade Group

The Frade Group is composed of the Santos, Jureia, Itajai-Acu Formations and Ilhabela Member. The tectonic phase corresponding to this group is the drift phase (Figure 10), associated with a marine abyssal environment (Chang et al., 2008). This group represents a regressive phase during which the shelf margin advanced up to 200 km basinward. It encompasses all sediments deposited from alluvial fan systems to bathyal pelites and sandstones, spanning from the top of the Cenomanian to the Cretaceous-Paleogene boundary (Moreira et al., 2007).

The Santos Formation, from the Cenomanian to the Cretaceous-Paleogene boundary, is characterized by reddish conglomeratic sediments of continental origin

and laterally interdigitating with the sediments of Jureia and Itajai-Acu (Moreira et al., 2007). It comprises the stratigraphic sequences K82-K86, K88, K100, K110 and K130.

The Jureia Formation occurs as sandy sediments, shales, siltstones, and clay-rich deposits laid down from continental environments to the more distal portions of the platform (Moreira et al., 2007). It comprises the stratigraphic sequences K82-K86, K88, K90, K100, K110 and K-130.

Moreover, Sequence K90 (Jureia, Itajai-Acu Formations and Ilhabela Member) corresponds to siliciclastic sediments from the Santonian to lower Campanian stages. Its lower boundary is the 85.6 unconformity (Santonian unconformity), and its upper boundary is the 79.2 Ma unconformity (Intra-Campanian I). The 85.6 Ma erosive event represents the most intense in the Santos Basin. According to Moreira et al. (2007), it is believed that the basin margin shifted westward of the Cretaceous hinge zone, as evidenced by the onlap of the Campanian and Maastrichtian sequence over these unconformities.

Interbedded with the deposits of the Jureia Formation, intense extrusive volcanism occurs. This Santonian volcanism is associated with an increased basin subsidence rate and with other volcanic and tectonic features present on the continent (the Rio Grande Uplift and the Cruzeiro do Sul Deformation Zone), along with the emergence of the Serra do Mar (Moreira et al., 2007). The Santonian depositional environment is characterized by slope and deep-basin settings, dominated by turbiditic deposits of the Itajai-Acu Formation.

The Itajai-Acu Formation is composed of siltstones and shales, as well as diamictites and marls deposited in distal platform, slope, and basin (abyssal) settings (Moreira et al. 2007). This Formation comprises the stratigraphic sequences K88, K90, K100, K110 and K130.

The Ilhabela Member is associated with sandstones from different depositional environments. For example, initially, in sequences K88 and K90, these sandstones are hyperpycnal flow deposits, that is, associated with river water. In sequence K80 and K90, these sandstones were deposited in an upper bathyal environment, while in K90 they are probably associated with a delta (Moreira et al. 2007), a shallower environment. The sandstones of the Ilhabela Member are highly significant in both area and thickness within sequence K90 (Moreira et al. 2007), which is an interesting

aspect. Meanwhile, from sequence K100 to K130, these sandstones are associated with strongly channeled, dense turbiditic flows related to major excavations on the slope and platform. The Ilhabela Member comprises the stratigraphic sequences K88, K90, K100, K110, K120 and K130.

3.2.5 Itamambuca Group

Itamambuca Group is composed of the Ponta Aguda, Marambaia, and Iguape Formations, Maresias Member, and Sepetiba Formation. The tectonic phase corresponding to this group is the drift phase (Figure 10). In addition, this group represents the sediments deposited after the Cretaceous-Paleogene boundary to the present day.

The Ponta Aguda Formation is characterized by reddish sandstones that overlies the unconformity that marks the boundary between the Paleogene and the Cretaceous (65,5 Ma) and is overlain by the unconformity at the lower boundary of the Pleistocene (1,6 Ma), which is related to a global eustatic fall. These sandstones are deposited in different depositional environments throughout sequences E10, E20, E30-E40, E50, E60, E70, E80, N10-N30, N40, and N50-N60. In sequences E10 and E20, the sandstones are deposited in alluvial fans, fluvial systems, and coastal deposits. In contrast, in sequences E30-E40, E50 and E60, they occur in platformal to continental environments. In the Lower Oligocene, following a significant relative sea-level rise that caused a marked retreat of the platform edge compared to sequence E60, these sandstones were deposited in coastal and continental settings. Later, from the Upper Oligocene to the Middle Miocene, in sequences E80 and N10-N30, they were deposited in platformal environments. It is worth noting that the upper boundary of sequence N10-N30 corresponds to a major unconformity representing a global eustatic fall (informally known as the “Gray Marker” in the Campos Basin) around 11 Ma (Moreira et al., 2007).

In sequence N40, the reddish sediments of the Ponta Aguda Formation have alluvial and coastal origin. It is important to highlight this stratigraphic sequence because it belongs to the interval from the Upper Miocene to the lower part of the

Miocene, corresponding to the time of the probable meteorite impact at Ilha do Mel crater. The stratigraphic sequence N40 has its lower boundary at the 11 Ma unconformity, which is related to a global eustatic fall (Gradstein et al. 2004 cited in Moreira et al. 2007), and its upper boundary at the 4.2 Ma unconformity. According to Peixoto (2004), as cited by Moreira et al. 2007, it is possible to correlate the Miocene erosion events with the formation of the East Antarctic Ice Sheet (11 Ma) and with the onset of Plio-Pleistocene glaciations (approximately 5 Ma). The depositional sequence N40 is composed of Ponte Aguda, Iguape and Marambaia Formations. In Iguape Formation, carbonates are interbedded with grayish-green mudstone, siltstone, and marls, and the Marambaia Formation comprises a large volume of debris flows composed of shale breccias and diamictites (Moreira et al. 2007).

The Marambaia Formation has been present since the early Paleocene (65,5Ma). It comprises siltstones and shales, in addition to diamictites and marls deposited in distal shelf, slope, and basin settings. It is defined from sequence E10 to N50-N60 (Moreira et al. 2007).

The Iguape Formation consists of calcarenites and calcirudites deposited near shelf break, with sedimentation occurring from the Oligocene (33.9 Ma) to the Pliocene. It is defined from sequence E70 to N50-N60 (Moreira et al. 2007).

The Maresias Member is characterized by sandstones resulting from strongly channelized high-density turbidite flows. These sandstones occur from the Paleocene (65.5 Ma) to the present day. They are defined within depositional systems sequences E10 to N50-N60 (Moreira et al. 2007).

The Sepetiba Formation is composed of gray to whitish sandstones, ranging from coarse to fine-grained, locally glauconitic, and of coquinas composed of mollusks, bryozoans, and foraminifera in the shelfal portion (Moreira et al. 2007). These deposits are Quaternary. It is included within stratigraphic sequence N50-N60.

Therefore, the probable Praia Grande impact structure, assigned to the Turonian in this study, and the Ilha do Mel structure, chronologically hosted between the Miocene and Pliocene (Menezes et al., 2012), are both associated with a marine depositional setting.

3.3 Petroleum system of the Santos Basin

The Santos Basin is a passive-margin basin situated in southeastern Brazil and currently represents the country's most productive oil basin (ANP, 2025). Although it is not the primary focus of this study, it is important to provide a brief overview of the region's petroleum system, particularly because petroleum systems have been documented in association with impact craters, such as the Ames crater in the United States (Carpenter et al., 1997) and the Siljan Ring in Sweden (Boden & Erikson, 1998 apud Juhlin, 2012).

The concept of a petroleum system, consolidated by Magoon & Dow (1994), defines a natural system that integrates the essential elements and processes required for the generation, accumulation, and preservation of hydrocarbons. According to Milani et al. (2000), a petroleum system is considered active when mature source rocks, seals, and traps operate synchronously, together with the time-dependent processes of migration and proper timing between hydrocarbon generation and trap formation.

The source rocks of the petroleum system in the Pre-salt section of the Santos Basin consist of organic rich lacustrine shales from the Itapema and Picarras Formations, deposited during the rift phase (Figure 12). The reservoirs are carbonates, composed of microbial-influenced limestones from the Barra Velha Formation and bivalve rudstones (coquinas) from the Itapema Formation. The main traps are associated with basement structural highs generated at the onset of the rift phase. During this phase, the faults responsible for hydrocarbon migration were also formed. The seal corresponds to the evaporitic package of the Ariri Formation, which can reach a thickness of over 2000 m.

On the other hand, the post-salt reservoirs are represented by the carbonates of the Guaruja Formation and turbiditic sandstones of the Itajai-Acu and Marambaia Formations (Figure 12). The main seal of the post-salt section consists of the siltstones and shales of the Marambaia Formation.

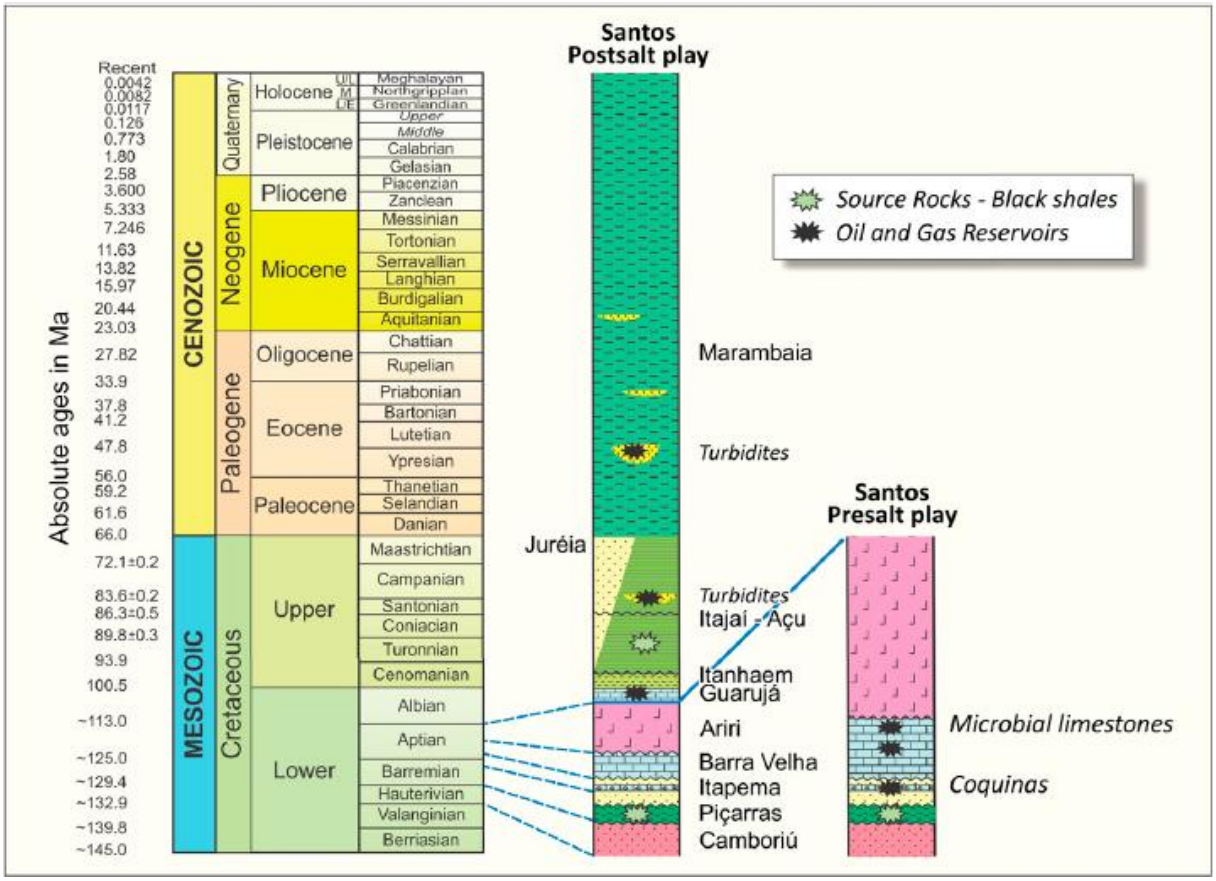


Figure 12. Simplified stratigraphy and comparison between the pre- and post-salt plays of Santos Basin (Baptista et al. 2023, after Moreira et al. 2007)

3.4 Turbidite systems

It is important to address turbidite systems, as the turbidite sandstones of the Itajai-Acu Formation represent significant post-salt reservoirs. In addition, turbidite systems can be triggered by tsunamis, which may or not be associated with meteorite impacts.

Turbidite systems correspond to sedimentary deposits formed by high-density gravity flows, typically associated with slope and deep-basin environments. These flows, also known as turbidity currents, transport and deposit sediments from the continental shelf to the deeper parts of the basin in response to sedimentary instability, tectonism, or eustatic variations (Mutti & Lucchi, 1972; Reading & Richards, 1994 cited in Barboza, 2025).

Turbidity currents are gravity flows typically composed of a basal granular layer and an upper, more dilute and turbulent layer. These flows may originate from short-lived catastrophic events, such as storms, earthquakes, or slope failures, as well as longer duration processes like major river floods. According to D'Ávila et al. (2008), a turbidity current can be subdivided into three main parts: the head, which is faster and thicker frontal portion where coarser grains are transported; the body, where the flow is relatively uniform; and the tail, characterized by rapid thinning of the flow and the dominance of finer sediments (Figure 13).

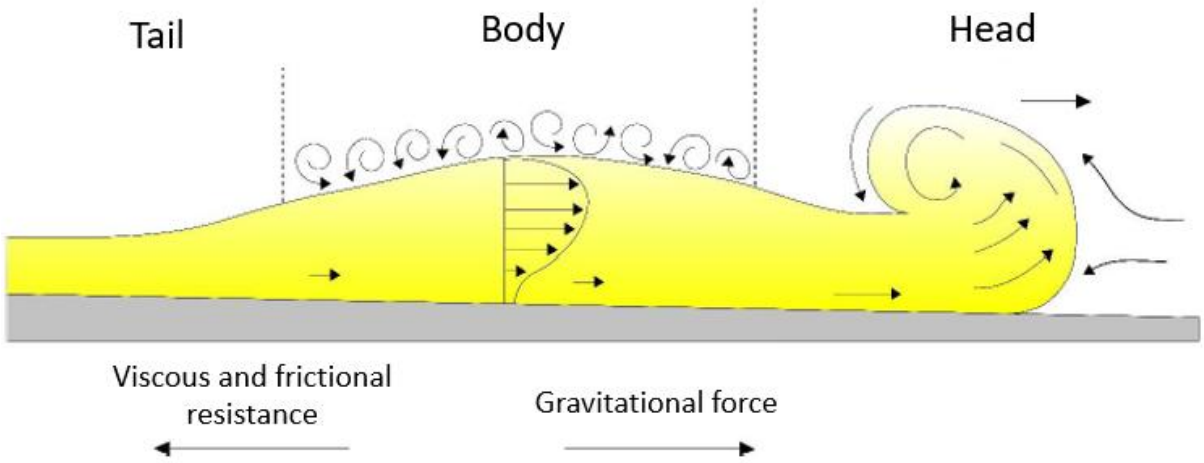


Figure 13. Schematic subdivision of a turbidity current (head, body, and tail). Modified from D'Ávila et al., 2008.

The head of a turbidity current is characterized by intense turbulence and erosion. Fine sediments suspended within the flow reduce basal friction, acting as a lubricating layer between coarser grains and allowing the current to travel longer distances. At the same time, muddy sediments increase the density of the flow and enhance turbulence in its upper part. Turbidity currents are commonly classified as high- or low-density depending on grain size, typically evolving from high-density to low-density flows during their development.

Due to the diversity and complexity of sedimentological processes, turbiditic deposits are often subdivided into depositional subsystems, based on lithological and/or geometrical/architectural elements variations within the sedimentary packages that make up the interval. In general, deep-marine deposits are characterized by two

main subsystems: channel-levee complexes and turbidite lobes. Figure 14 shows the schematic depositional model of turbiditic deposits proposed by Mutti et al. (1999). Figure 15 represents a schematic section of the facies and predominant grain sizes found throughout the turbidite deposits.

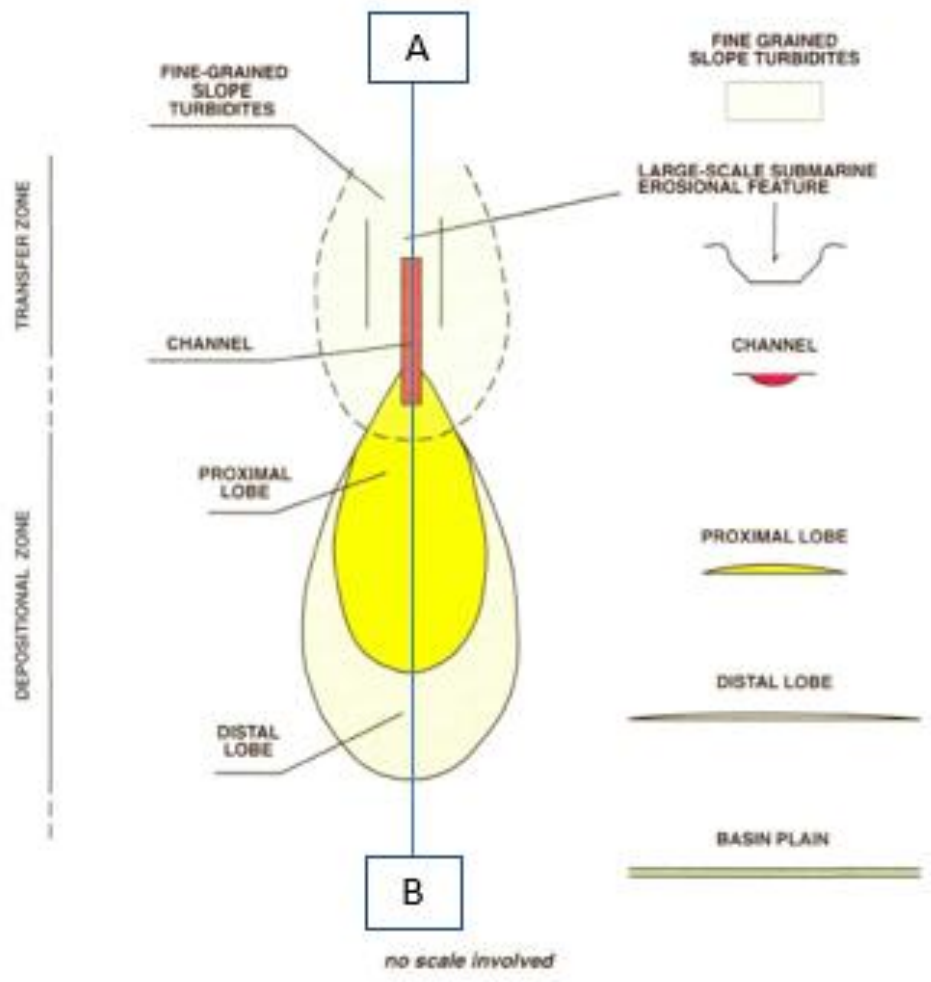


Figure 14. Conceptual diagram showing the main elements of a turbidite depositional system (Modified from Mutti, 1999).

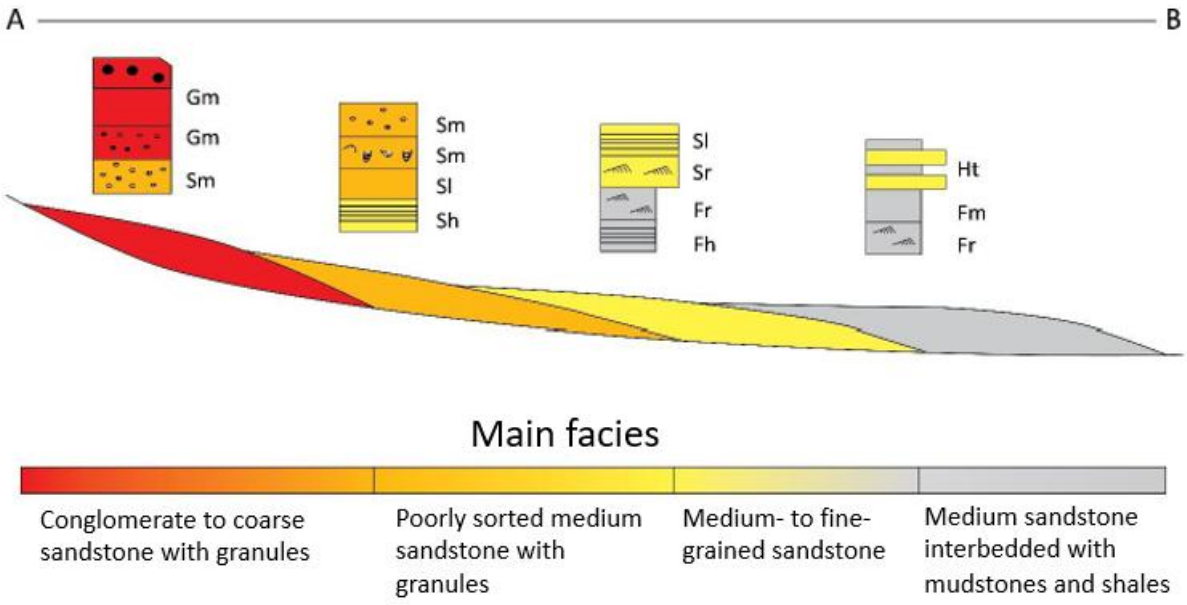


Figure 15. Distribution of the main faces and dominant grain size according to the depositional model for high-efficiency turbidite systems (modified from Mutti, 1999 by Morais, 2017, and translated into English in this work).

4. LITERATURE REVIEW

4.1 Seismic Reflection Method

The seismic reflection method plays a central role in hydrocarbon exploration. Since the 1930s, it has been the most widely used geophysical technique (Reynolds, 2011) owing to its high resolution, significant depth of investigation, and relatively high accuracy (Telford, 1990). Exploration seismology originated from earthquake seismology and relies on fundamentally similar measurement principles. However, despite the similarities in data acquisition parameters, the energy sources differ. Earthquake seismology uses naturally occurring seismic waves to investigate the physical properties of the Earth, whereas exploration seismology employs artificially generated elastic waves produced by controlled and mobile sources (Sheriff, 1995).

The travel times, amplitudes, and reflection angles of these waves, such as compressional (P) waves, are recorded by receivers at the surface (Figure 16). In marine environments, these receivers are hydrophones, while on land they are

geophones. The recorded data are subsequently processed and interpreted to infer physical properties and geometries of subsurface geological structures (Taner, 2001; Reynolds, 2011).

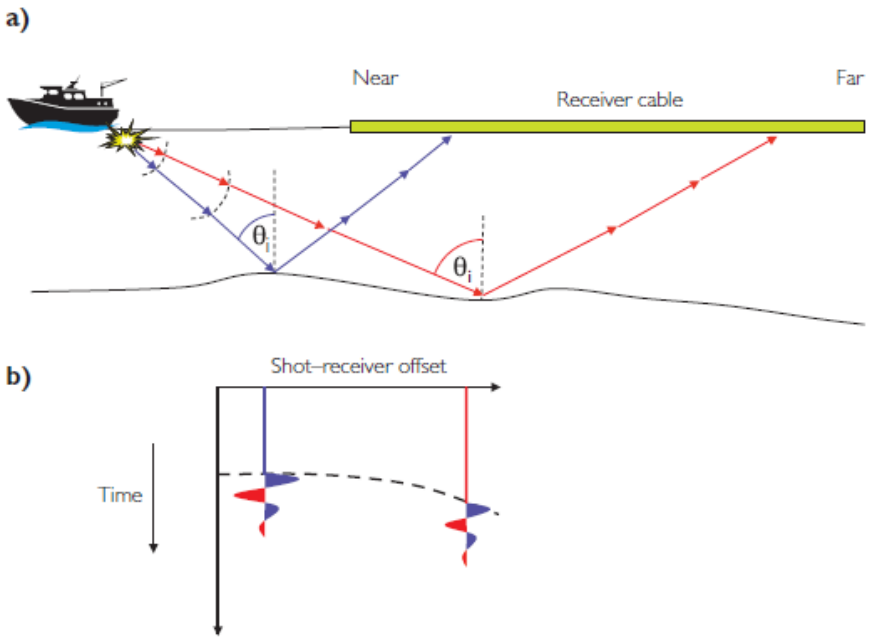


Figure 16. Marine seismic geometry: (a) source-receiver configuration illustrating wavefronts and rays (perpendicular to the wavefronts), with the angle of incidence increasing as offset increases; (b) shot gather representation of recorded energy. In a horizontally layered medium, reflections describe a hyperbolic trajectory on the gather. The reflection amplitude is controlled by the acoustic contrast across layer boundaries and by geometric spreading, which causes amplitude decay with increasing travel distance (Simm & Bacon, 2014).

In seismic reflection surveys, the distribution of reflected and transmitted energy at an interface is governed by contrasts in acoustic impedance between adjacent layers. This relationship is quantified by the reflection coefficient, which is given by the Zoeppritz equations (Equation (1); Zoeppritz, 1919 apud Kearey, 2002). For normal incidence, these equations reduce to the following simplified expression:

$$R = \frac{\rho_2 v_2 - \rho_1 v_1}{\rho_2 v_2 + \rho_1 v_1} = \frac{Z_2 - Z_1}{Z_2 + Z_1} \quad (1)$$

Acoustic impedance is defined as the product of P-wave velocity (v) and its bulk density (ρ). The propagation of a P-wave will depend on the bulk and shear elastic moduli, as well as the density of the material (Kearey, 2002).

Figure 17 schematically illustrates the convolutional model, in which the seismic trace is obtained by convolving the reflectivity series (R) with a seismic wavelet.

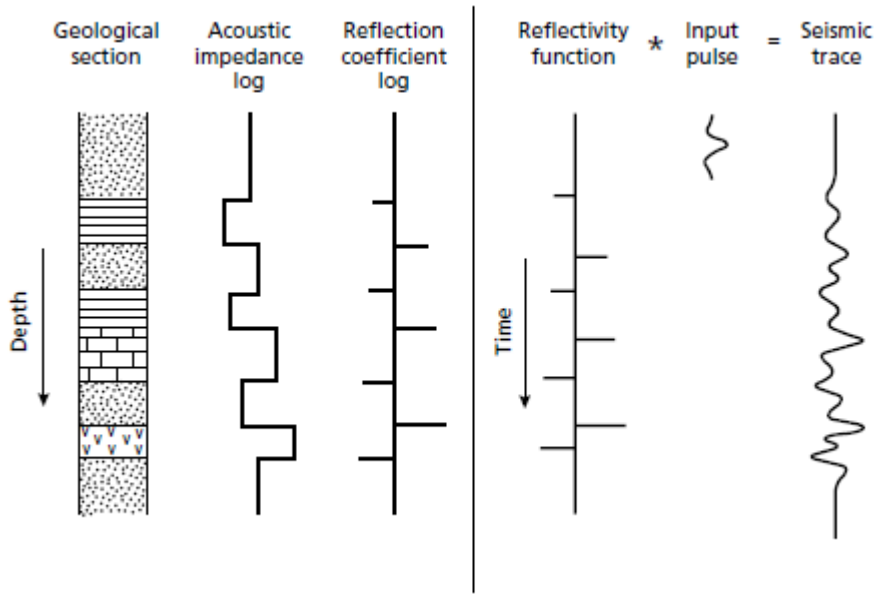


Figure 17. The convolutional model of the reflection seismic trace, showing the trace as the convolved output of reflectivity function with an input pulse, and the relationship of the reflectivity function to the physical properties of the geological layers (Kearey, 2002).

4.2 Seismic Processing

Through the acquired seismic data, seismic processing must be carried out to enhance the signal-to-noise ration and to obtain more reliable estimates of subsurface layer velocities (Yilmaz, 2001). This procedure enables the extraction of essential information for the geological interpretation of the processed seismic section.

The seismic processing workflow can be adapted according to the objectives and criteria of the interpreter (Yilmaz, 2001). Consequently, it comprises several stages. The typical sequence of seismic data processing includes geometry assignment, noise attenuation, deconvolution, velocity analysis, NMO correction (Normal Moveout), stacking, and migration. However, since the focus of this study is the application of seismic attributes to an already processed seismic volume, only the final step, migration, will be briefly discussed.

4.2.1 Migration

According to Schulte (2012), migration is the process by which seismic data are correctly positioned in the subsurface by relocating events to their true spatial locations. For example, by applying a suitable Green's function (Equation(2)), Santos et al. (2020) migrated their seismic data (Figure 18). A suitable Green's function, is short, is dependent on the correct velocity field. For time migration, one may use a Rayleigh II integral to backpropagate wavefield U recorded at the surface z_o, where $U_{mig}(x_i,y,z_o,t)$ is the recorded wavefield at a horizontal surface z_o, and G^* is the conjugate of the Green's function.

$$U_{mig}(x_i, y_i, z_o, t) = \frac{1}{2\pi}\int_{-\infty}^{+\infty}\int_{-\infty}^{+\infty} U(x, y, z_o, t) * \frac{dG^*}{dz}\, dxdy \tag{2}$$

In Figure 18 the focal point can be observed, where diffracted waves converge to form a single reflector. Therefore, the velocity used in case (d), 2000 m/s, represents the most appropriate migration velocity, as determined through diffraction velocity analysis during the migration process.

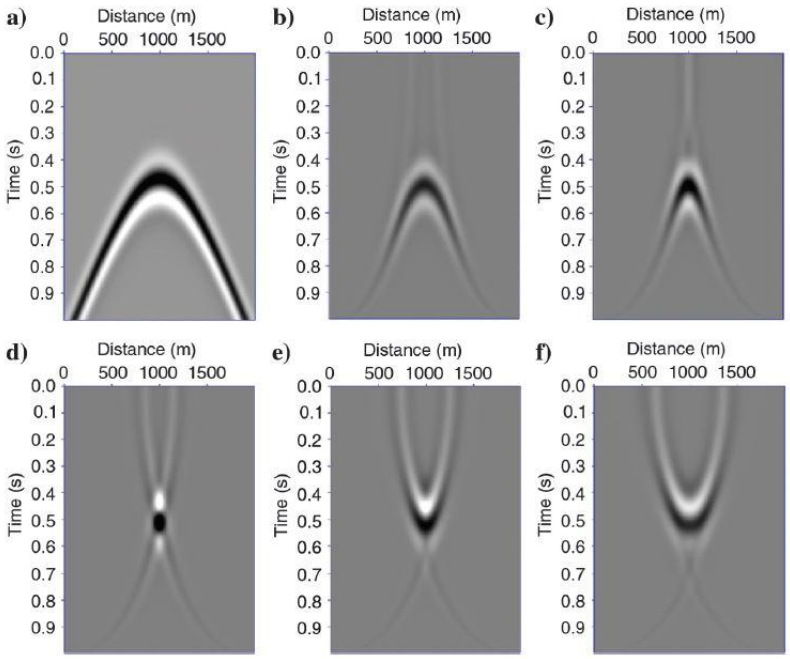


Figure 18. (a) Seismogram and (b-f) the migration results of increasing the velocity from 1500 m/s to 2500 m/s at each 250 m/s increment. Equation 2 is used for zero-offset migration (Santos et al. 2020).

4.3 Seismic Attributes

Seismic attributes are primary tools used to infer lithology from seismic reflection data and to support reservoir characterization. They can also be regarded as filters that quantify specific properties of seismic images and enhance geological features of interest (Taner, 2001; Barnes, 2016).

Based on Barnes (2016, p.13), the history of seismic attributes began in the 1950s with the earliest efforts to extract geological information from seismic reflection character. Figure 19 provides a brief overview of the historical evolution of seismic attributes from 1960s onward. According to Chopra & Marfurt (2005), several of the most important seismic attributes were developed well before the advent of digital recording, during the era of paper records, including frequency analysis used to optimize filter settings in magnetic analog recordings (Anstey, 2005). As illustrated in Figure 19, after 1970 seismic attributes began to be commercially displayed in color (Balch, 1971 apud Taner et al., 1979), and complex trace analysis was introduced. The complex trace allowed the distinct separation of envelope amplitude and phase components, as well as the computation of instantaneous frequency, while color seismic sections enhanced the interpreter´s ability to recognize spatial variations (Taner et al., 1979). Since then, seismic attributes and their applications have continued to evolve to the present day.

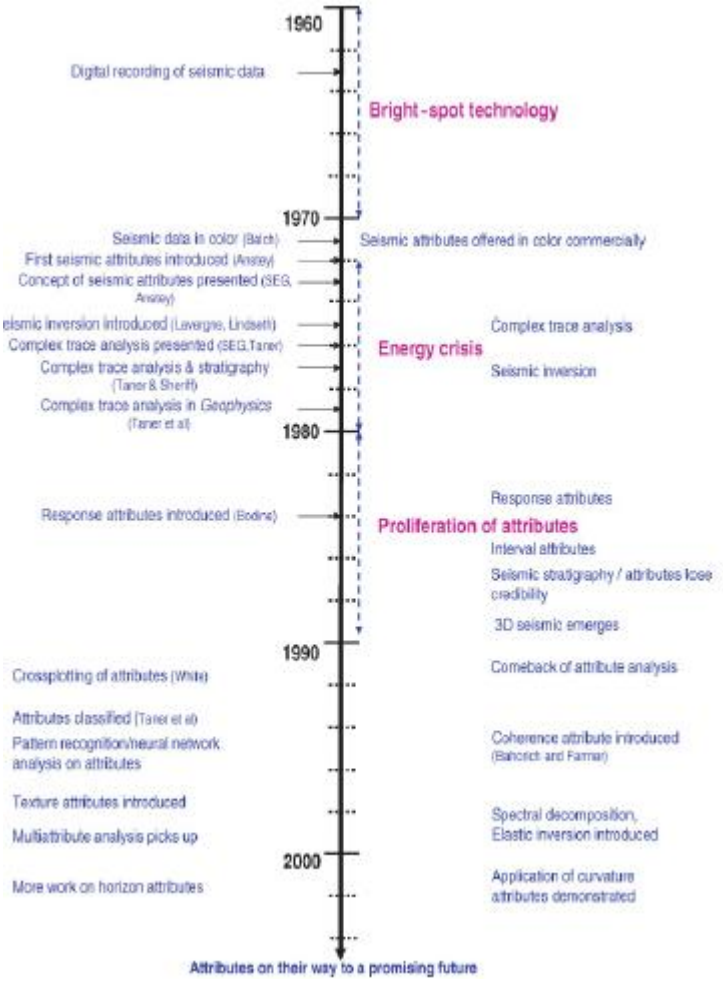


Figure 19. A time line of seismic attribute developments and their relationship to key advances in seismic exploration technology (after Barnes (2001) as cited in Chopra & Marfurt (2005)).

Barnes (2016) categorized seismic attributes based on the properties they measure into three types: geological, geophysical, and mathematical (Figure 20). Geological attributes characterize structural features, such as dip, azimuth, curvature, and discontinuity. Geophysical attributes describe the properties of seismic waves and wavelets, including amplitude, phase, frequency, and bandwidth. Mathematical attributes are generally less informative from a geological point of view, as they lack inherent geological significance; they represent statistical measures of seismic data, such as averages, variances, counts, and ratios.

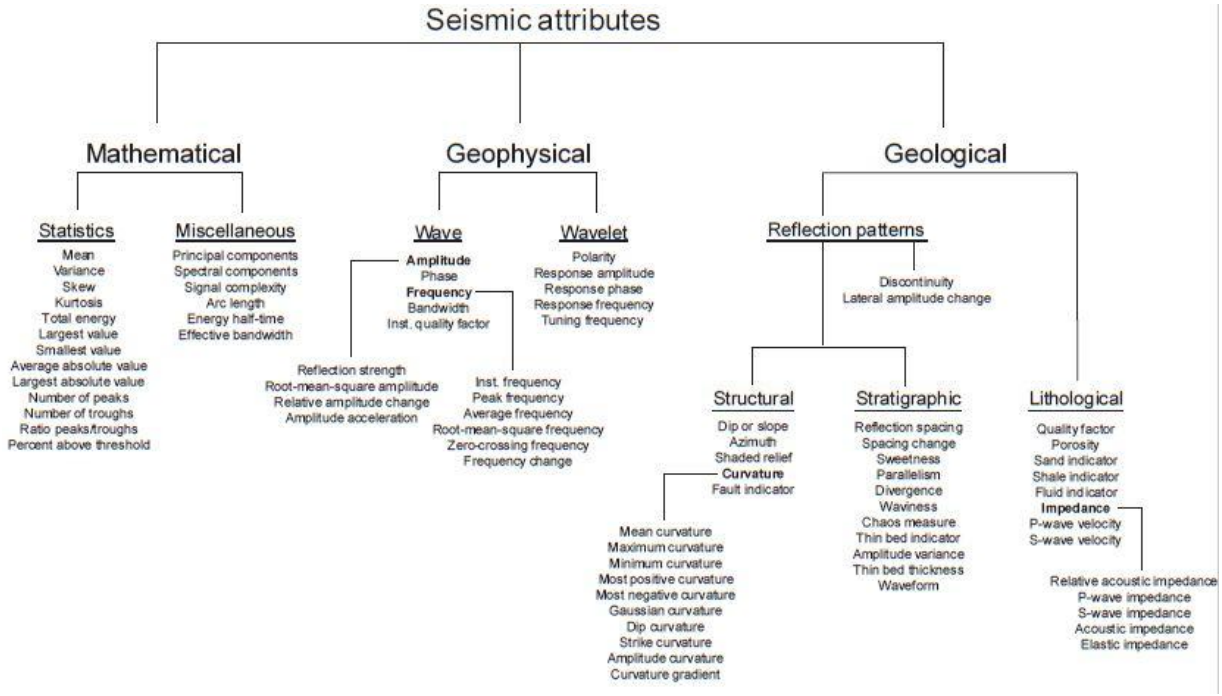


Figure 20. Seismic attributes categorized by property (Barnes, 2016, p.5)

Seismic attributes can be represented as maps, cross-sections, or volumes. Maps are the most commonly used format due to their ease of interpretation and relatively low computational cost. Attribute maps are typically derived from seismic horizons and can be calculated at the horizon itself, in which case they are considered horizon attributes, or sometimes as surface attributes.

The following subsections will discuss some of the attributes that will be evaluated in this study, according to the classification in Figure 20. Since the geological attribute sweetness is defined as the ratio between the geophysical attributes Reflection Strength and Instantaneous Frequency, these will also be addressed separately.

4.3.1 Amplitude Envelope

The amplitude envelope, also referred to as *reflection strength, instantaneous amplitude*, or *instantaneous envelope*, is a complex trace seismic attribute (Figure

21; Taner et al., 1979). It is defined by Equation (3). In this formulation, *f(t)* represents the real seismic trace, whereas *q(t)* corresponds to the quadrature trace.

$$A(t) = (f(t)^2 + q(t)^2)^{\frac{1}{2}} \quad (3)$$

The amplitude envelope seismic attribute measures the total instantaneous energy and is directly related to acoustic impedance contrasts. However, a limitation of this attribute is that it reduces the vertical resolution of the seismic data (Chen and Sidney, 1997).

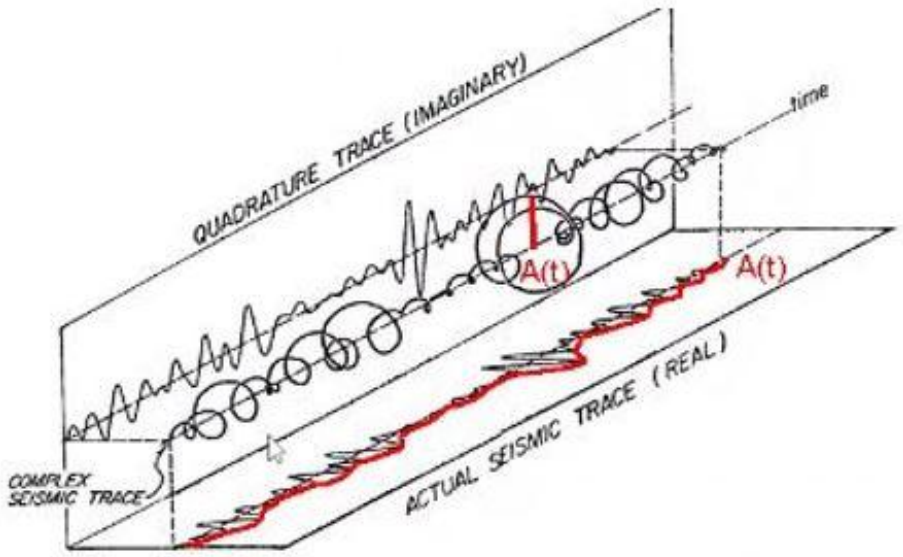


Figure 21. Isometric diagram of portion of an actual seismic trace. Amplitude envelope is highlighted in red (after Taner et al., 1979).

4.3.2 Instantaneous Frequency

Instantaneous Frequency is a complex trace attribute defined (Figure 22d) as the time derivative of instantaneous phase (Figure 22c), expressed as $d_y(t)/f(t)$, and typically measured in degrees/ms or radians/ms (Chen & Sidney, 1997). This attribute is particularly useful for identifying stratigraphic discontinuities and for estimating seismic attenuation caused by hydrocarbons (oil and gas) reservoirs, which often

results in a reduction of high-frequency components (Chen & Sidney, 1997). Consequently, it can aid in detecting anomalous attenuation and thin-bed tuning effects (Chopra & Marfurt, 2007).

In addition, according to Taner (2001), instantaneous frequency may serve as an indicator of fractured zones, as fractured intervals commonly appear as lower-frequency anomalies.

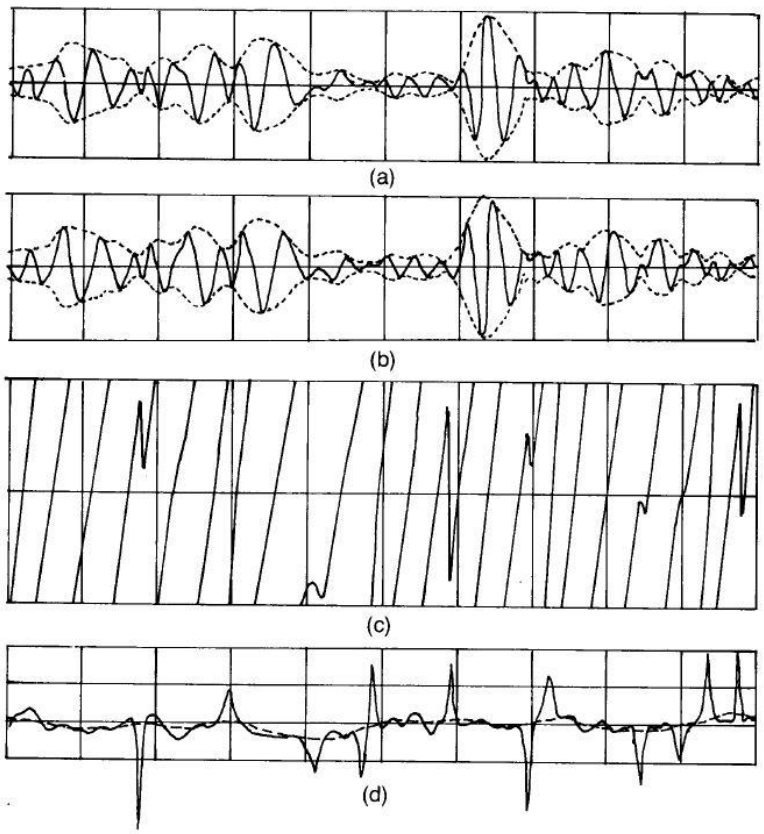


Figure 22. Real (a) and quadrature (b) traces for a portion of an actual seismic trace. Also shown is the envelope [dotted curve in (a, b)], phase (c), instantaneous frequency (d), and weighted average frequency [dotted curve in d] (Taner et al., 1979).

4.3.3 Sweetness

Sweetness is an empirical attribute calculated as the ratio between the amplitude envelope (*A(t)*) and the square root of the instantaneous frequency (*F(t)*) (Equation (4)).

$$\text{Sweetness (t)} = \frac{A(t)}{\sqrt{F(t)}} \quad (4)$$

As previously discussed, the amplitude envelope (A(t)) is defined as the square root of the sum of the squared amplitudes of the real and imaginary traces and represents the total seismic energy within a predefined interval (section 4.3.1). Consequently, horizons characterized by higher amplitudes and lower frequencies (typically associated with sandy intervals) exhibit higher sweetness values, whereas sediments with lower amplitudes and higher frequencies (commonly related to finely laminated shales) present lower values (Hart, 2008). This attribute is classified as a geological attribute due to its stratigraphic significance (Figure 20).

4.3.4 Root-mean-square amplitude

Root-mean-square (RMS) amplitude is a seismic attribute that represents the magnitude of seismic trace values or their envelope. It quantifies the average energy variation within a defined time window between horizons or throughout a seismic volume (Barnes, 2016). Because RMS amplitude is always positive, it enhances both positive and negative peak amplitudes and is independent of data polarity or phase.

The RMS amplitude attribute is computed as the square root of the sum of squared amplitudes divided by the number of samples within a given time window:

$$X_{rms} = \sqrt{\frac{1}{N}\sum_{n=1}^{N} x_n^2} \quad (5)$$

This single-trace, window-based attribute is effective for identifying bright spots associated with gas accumulations, tuning effects, hard streaks, or porosity variations (Barnes, 2016), as well as for tracking lithologic changes such as deltaic channels and gas sands (Chen & Sidney, 1997).

4.3.5 Relief

Relief, pseudo-relief, or tecVA (Amplitude Volume Technique) consists of applying a -90º phase shift to the RMS amplitude. The Amplitude Volume Technique (técnica Volume de Amplitudes – tecVA) was first proposed by Bulhões (1999) and later extended by Bulhões and de Amorim (2005), allowing its application to seismic volumes in both time and in depth, based on the concept of the elementary seismic bed. The elementary seismic bed corresponds to the thinnest layer resolvable by the seismic data, and its thickness *M*, which is half of the shortest period (highest frequency), is used as a weighting factor in the tecVA calculation (Bulhões and de Amorim, 2005).

The technique involves applying an inverse Hilbert Transform to either the average Root-Mean-Square (RMS) amplitude or the average of the absolute amplitudes, effectively implementing a -90º phase shift in RMS amplitude attribute (Figure 23). To do this, you first need to choose the window (M) in time or depth to be used in calculating the average RMS (Bulhões and de Amorim, 2005). The choice of this window is a decisive moment, because it will be responsible for the resolution of the seismic data. For example, according to Vernengo and Trinchero (2015), when the mobile window is very long, the result of the RMS calculation will be perceived as a more softened trace with an aspect similar to that an envelope. Whereas when the window is shorter, the aspect is different and the resolution is better (Barnes, 2016; Vernengo & Trinchero, 2015).

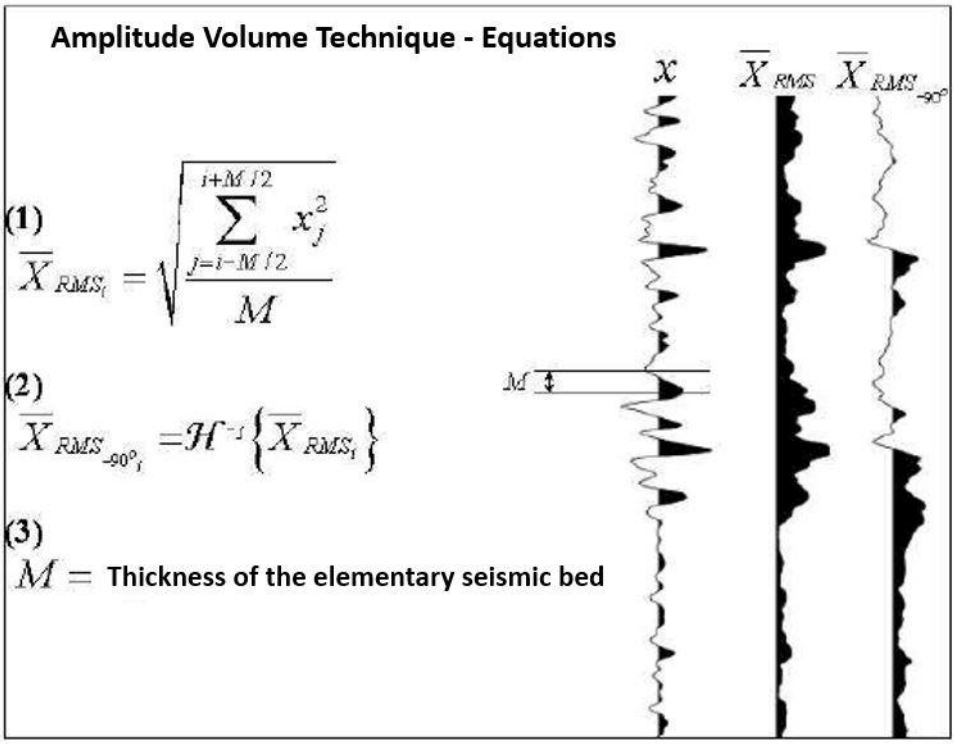


Figure 23. Formula of the Amplitude Volume Technique, where (1) is the RMS average, (2) is the inverse Hilbert Transform with a -90º phase rotation, and (3) is the window size, corresponding to the elementary seismic bed (after Bulhões and de Amorim, 2005).

4.3.6 Coherence

The coherence is classified as a geological attribute of discontinuity (Figure 20). According to Marfurt (2018), coherence algorithms can be broadly classified into two categories: those sensitive only to lateral variations in waveform, and those sensitive to lateral variations in both waveform and amplitude. Cross-correlation, eigenstructure, and energy-ratio coherence algorithms belong to the first category, whereas semblance, Sobel filters, and chaos algorithms fall into the second (Marfurt, 2018).

In this section, the seismic coherence attribute based on the semblance algorithm is presented, as it was the method applied in this study. According to Marfurt (2018), Marfurt et al. (1998) proposed a semblance estimate of coherence c_{semb} computed from M traces and 2K+1 samples, originally defined as Equation (6).

(6)

$$c_{semb} = \frac{\sum_{k=-K}^{+K}\left\{\frac{1}{M}\sum_{m=1}^{M}[d(t_k, x_m, y_m)]\right\}^2}{\frac{1}{M}\sum_{k=-K}^{+K}\{\sum_{m=1}^{M}[d(t_k, x_m, y_m)]^2\}}$$

The coherence is particularly effective for fault detection, as fault-related displacement causes trace misalignment and, consequently, reduced coherence values. Coherence values close to 1 indicate similar traces and preserved continuity, whereas coherence values close to 0 indicate dissimilar traces, reflecting geological discontinuities.

4.3.7 Relative Acoustic Impedance

Relative acoustic impedance is obtained by integrating the real part of the seismic trace (Taner, 2001; Emujakporue & Enyenihi, 2020).

$$\ln(\rho v) = 2\int_{t=0}^{t=T} f(T)dt \tag{7}$$

As a result, this attribute provides a relative estimate of impedance variations, highlighting lithological contrasts, although absolute impedance values cannot be retrieved without well calibration.

5. DATA AND METHODS

5.1 Seismic database

Our dataset consists of two post-stack seismic volumes in the time domain acquired by Petrobras and provided by ANP (Agência Nacional do Petróleo, Gás Natural e Biocombustíveis). The data were imported into Aspentech/Paradigm software for interpretation. In the Ilha do Mel survey, inlines and crosslines are oriented in the N-S and W-E directions, respectively, with spacings of 25.0 m (inlines) and 12.5 m (crosslines), and a sampling interval of 4 ms. In contrast, the Praia Grande survey has inlines and crosslines oriented W-E and NNW-SSE, respectively, both spaced at 25.0 m, with a sampling interval of 4 ms. Figure 24 shows the flowchart of the methodology used in this study. Before applying the seismic attributes, the seismic volume was cropped to reduce computational cost. Thus, the Praia Grande area become equivalent to 7677,5 km^2 and the Ilha do Mel area correspond to 3839 km^2.



Figure 24. Flowchart of the methodology used in this study.

The three-dimensional reflection seismic data from Praia Grande were acquired and processed in 2004 for petroleum exploration of a block in the exploratory phase, under the Petrobras' concession in the Santos Basin (Correia et al., 2005). Well 1-SPS-31, drilled in 1989 prior to this acquisition, was even imported into Aspentech/Paradigm software for interpretation. However, although it was imported, it lacked a checkshot, did not intersect the entire stratigraphic of the Praia Grande structure and was not used in this study.

5.2 Seismic interpretation and seismic attributes application

The horizons and faults of the Ilha do Mel survey were interpreted at intervals of 175m along the inlines and 87.5 m along the crosslines. In contrast, the horizons and faults of the Praia Grande survey were interpreted at intervals of 375 m and 175 m, respectively.

To support the interpretation, five seismic attributes were applied - coherence cube, RMS amplitude, relief, sweetness and relative acoustic impedance - using the standard implementation of the seismic interpretation software (Aspentech/Paradigm) and were analyzed qualitatively for interpretation purposes. The algorithms behind these applications were discussed in sections 4.3.6, 4.3.4, 4.3.5, 4.3.3, and 4.3.7, respectively.

6. RESULTS

6.1 Ilha do Mel Structure

6.1.1 Seismic-stratigraphy and structural framework

In the Ilha do Mel impact structure, three horizons were interpreted (H1, H2, and H3), following the work of Menezes et al. (2012). These horizons represent the strongest reflectors within the crater region (Figure 25). As reported by Menezes et al. (2012), Ilha do Mel is interpreted as a complex impact structure with an approximate diameter of 6 km. All horizons are reported in two-way travel time (TWT), as seismic velocity data were not available for accurate depth conversion.

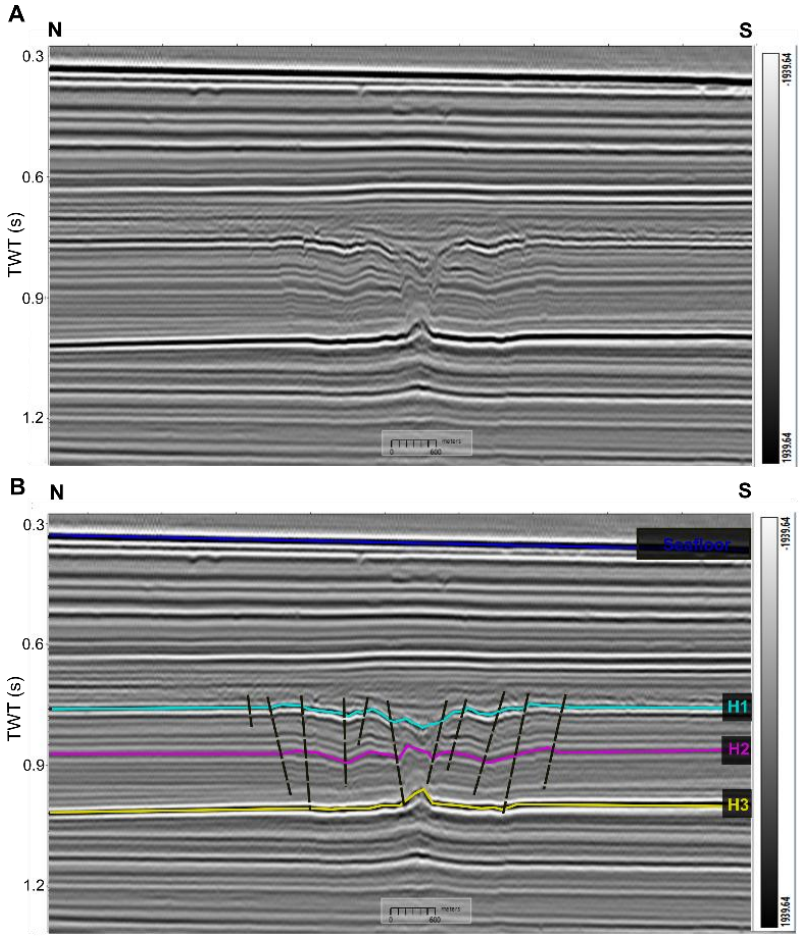


Figure 25. Seismic inline 1246 showing interpreted horizons (H1, H2, and H3) and faults.

After the seismic attribute analysis, faults were mapped across the Ilha do Mel structure (Figure 26). Concentric normal faults are observed at all interpreted horizons (H1, H2, and H3; Figures 29-31), defining an annular structural pattern around a central disturbed zone. The fault network is best developed at the H1 horizon, where faults are more abundant and better defined, whereas at deeper horizons (H2 and H3) the structures become less pronounced. In addition to the main structure, several smaller circular depressions are observed around the central feature, characterized by localized reflector disruption and circular geometries.

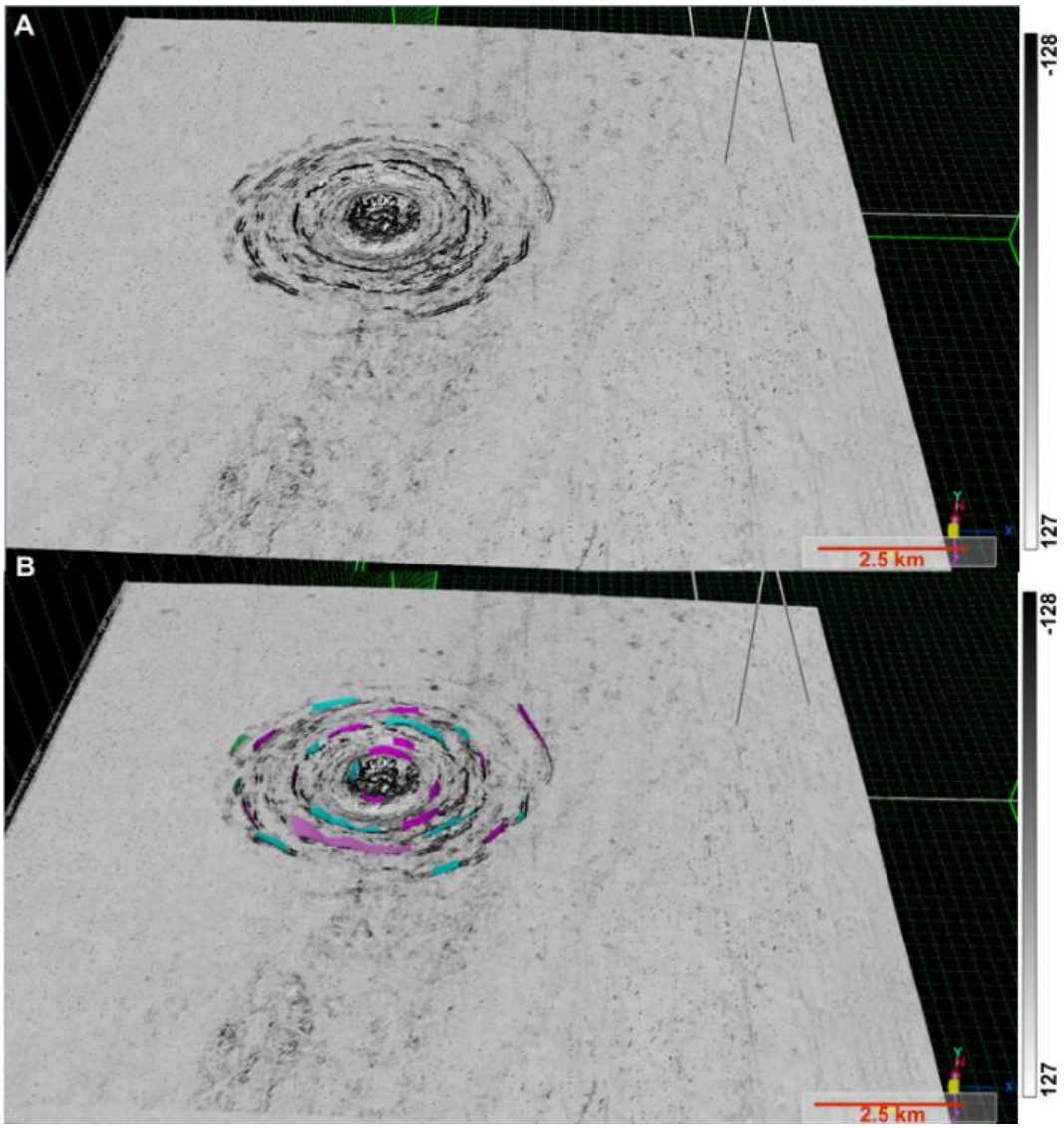


Figure 26. Interpreted faults on the H1 horizon slice overlain on the coherence cube.

Figure 27 presents a three-dimensional visualization of integrated geophysical data, focusing on the structural deformation above the H2 horizon slice of the Ilha do Mel impact crater. The interpretation integrates seismic attribute slices with structural fault mapping. The extensive, flat surface rendered in grayscale represents the mapped stratigraphic horizon (Horizon H2). Its fine-grained texture and variations in gray tones result from applying a seismic coherence algorithm, an attribute highly effective at highlighting horizontal discontinuities. Outside the impact zone, the response is homogeneous (flat and continuous), whereas in the central portion, the seismic signature changes drastically, revealing the disruption and loss of layer continuity caused by post-impact collapse.

A well-defined circular depression is visible at the center of the horizon, surrounded by a concentric, annular geometric pattern. The vertical to inclined, blade-like features in magenta and light blue represent the interpreted tectonic fault planes. These are predominantly listric normal faults (ring faults) that developed immediately after the impact during the crater modification stage, when the unstable rims generated by the blast collapsed toward the center under gravity.

To the right, a vertical color bar ranging from black to white (with indicative values from -128 to 127) represents the numerical limits of the coherence attribute used on the H2 slice, where discontinuities are represented by the black peak (-128). The dark background with green gridlines serves as the 3D bounding box within the geological interpretation software."

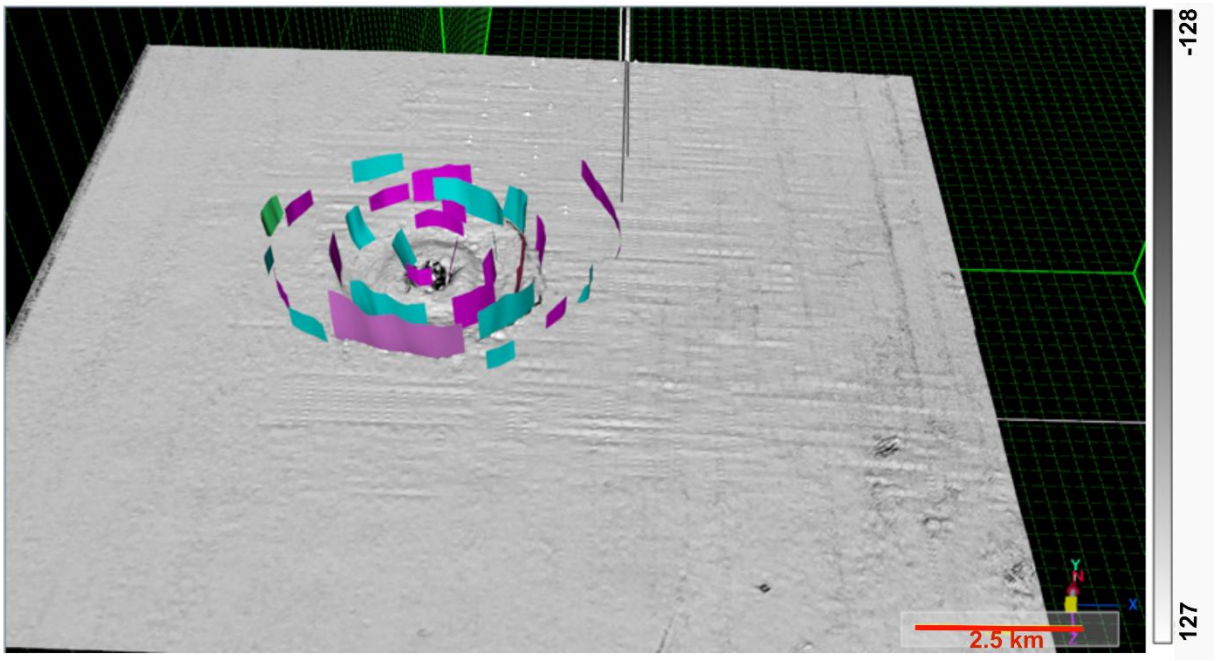


Figure 27. Interpreted faults on the H2 horizon slice overlain on the coherence cube.

Figure 28 presents a 3D visualization focused on a different stratigraphic level, the H3 horizon slice, detailing the continuous structural deformation caused by the impact crater. In the central impact zone, the seismic coherence attribute records an abrupt drop, displayed as concentric circular patterns in dark and black tones. This indicates zones of severe discontinuity, where the original stratal arrangement was highly fractured, displaced, or rotated due to the impact and subsequent gravitational accommodation.

The 3D surfaces, displayed as vertical to inclined blade-like features in magenta and light blue, continue to delineate the normal ring fault system. In this visualization, it is possible to observe in detail how these faults geometrically crosscut and intersect the H3 surface. At the base of some fault planes, a subtle intersection outline delineates the blocks that collapsed inward toward the crater center.

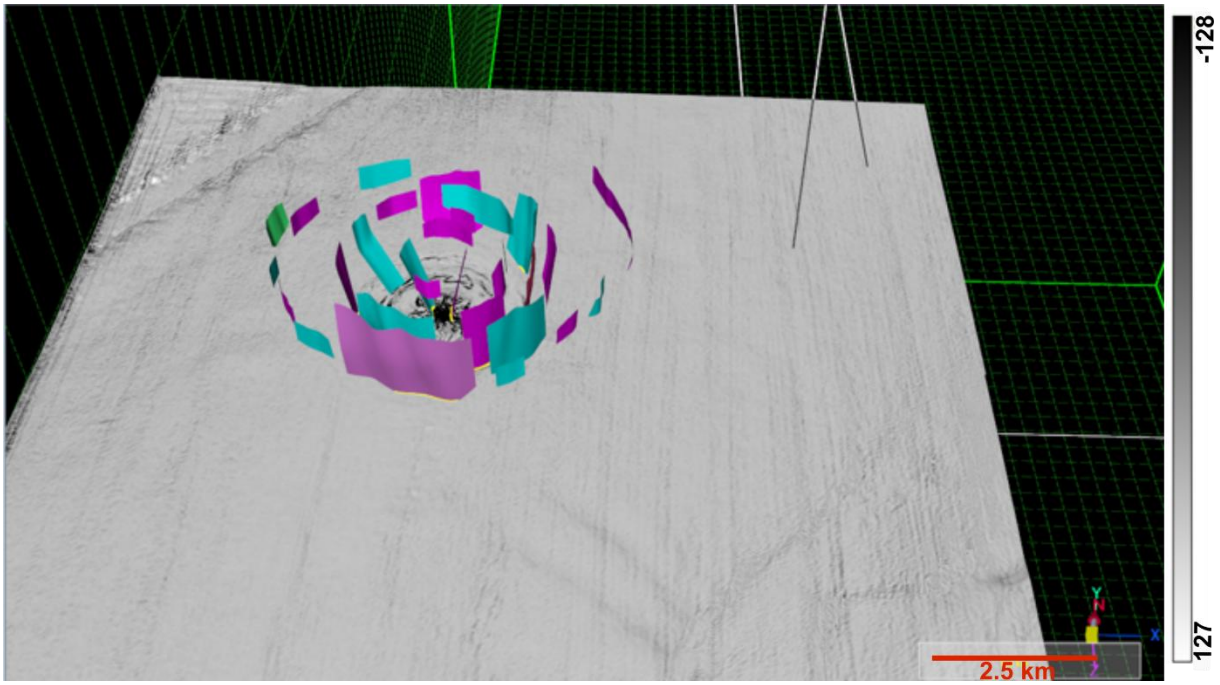


Figure 28. Interpreted faults on the H3 horizon slice overlain on the coherence cube.

6.1.2 Attribute analysis on mapped horizons

In the Ilha do Mel impact structure, three horizons were interpreted: H1, H2, and H3. Figure 29 shows five seismic attributes (B-F) applied to the H1 horizon slice (A). The coherence cube highlights concentric normal faults and potentially smaller circular depressions, which may correspond to secondary impact features generated by ejected material rather than simple pockmarks.

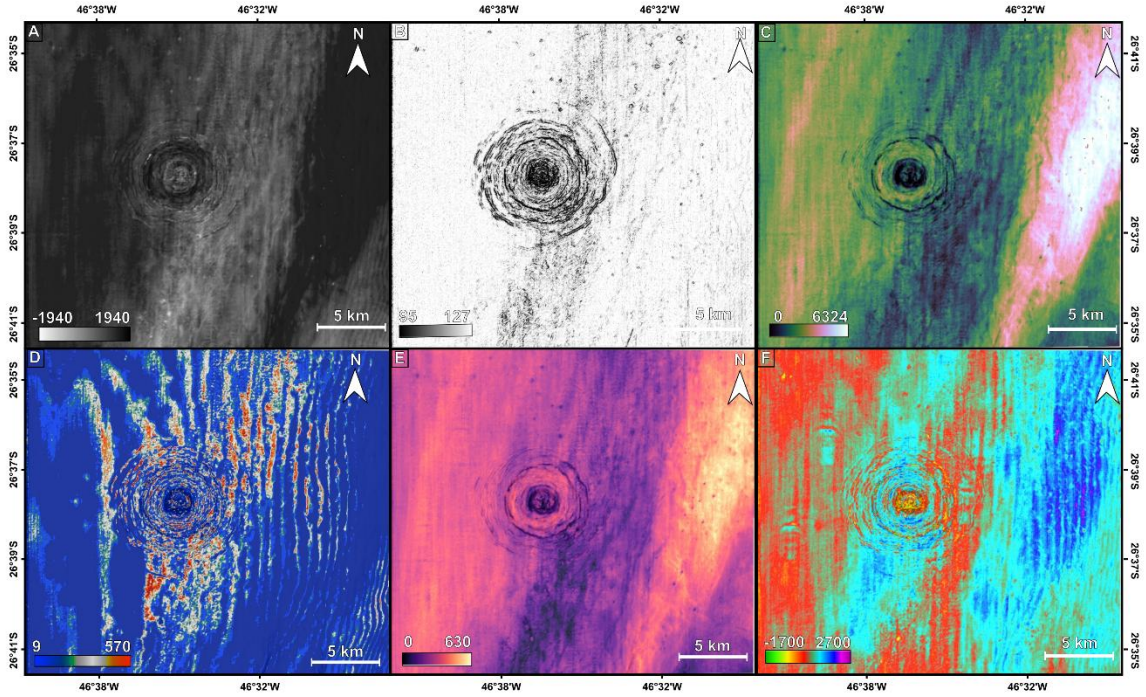


Figure 29. Composite maps from a horizon slice near the top of the structure designated as H1 horizon slice (A), coherence cube (B), RMS amplitude (C), relief (D), sweetness (E), and relative acoustic impedance (F).

On the right side of the crater (N-SW), a zone of increased RMS amplitude, relative acoustic impedance, and sweetness is observed. The relief attribute highlights the western portion of the crater more clearly than the other seismic attributes.

Figure 30 shows five seismic attributes (B-F) applied to the H2 horizon slice (A). In these horizon, RMS amplitude (C) and sweetness (E) display similar responses, highlighting comparable lithological variations. Among all attributes, the coherence cube proved to be the most effective in delineating the impact structure.

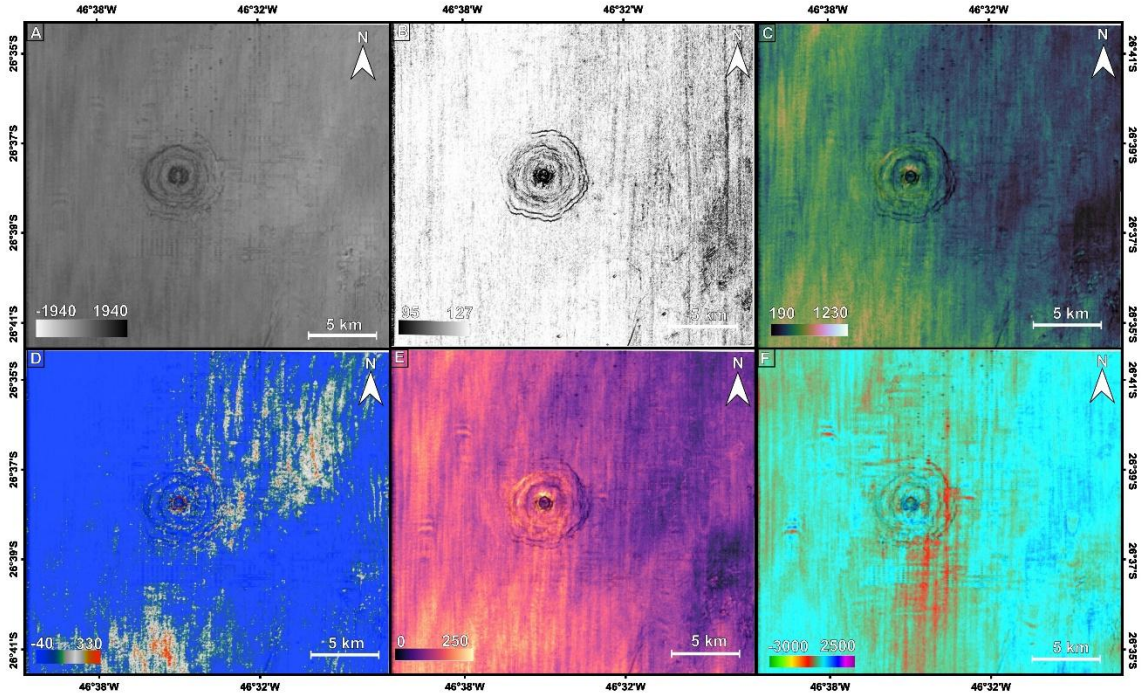


Figure 30. Composite maps from a horizon slice near the top of the structure designated as H2 horizon slice (A, seismic section without attributes) and its seismic attributes: coherence cube (B), RMS amplitude (C), relief (D), sweetness (E), and relative acoustic impedance (F).

Figure 31 shows five seismic attributes (B-F) applied to the H3 horizon slice (A). A lagoon is observed in the top-left corner, to the north. In Figure 30A, the circular feature of the crater is subtly visible in the center of the image as a series of concentric rings of a dark-gray hue, slightly contrasting with the homogeneous background. In the H3 horizon slice with the relief seismic atribute (Figure 31 D), the circular structure interrupts the regional trend of northeast-southwest-trending lineaments. It is expressed in the center as a set of perfect concentric rings with rough, concentric relief (alternating red and blue), highlighting the ridges and depressions of the crater rim and interior.

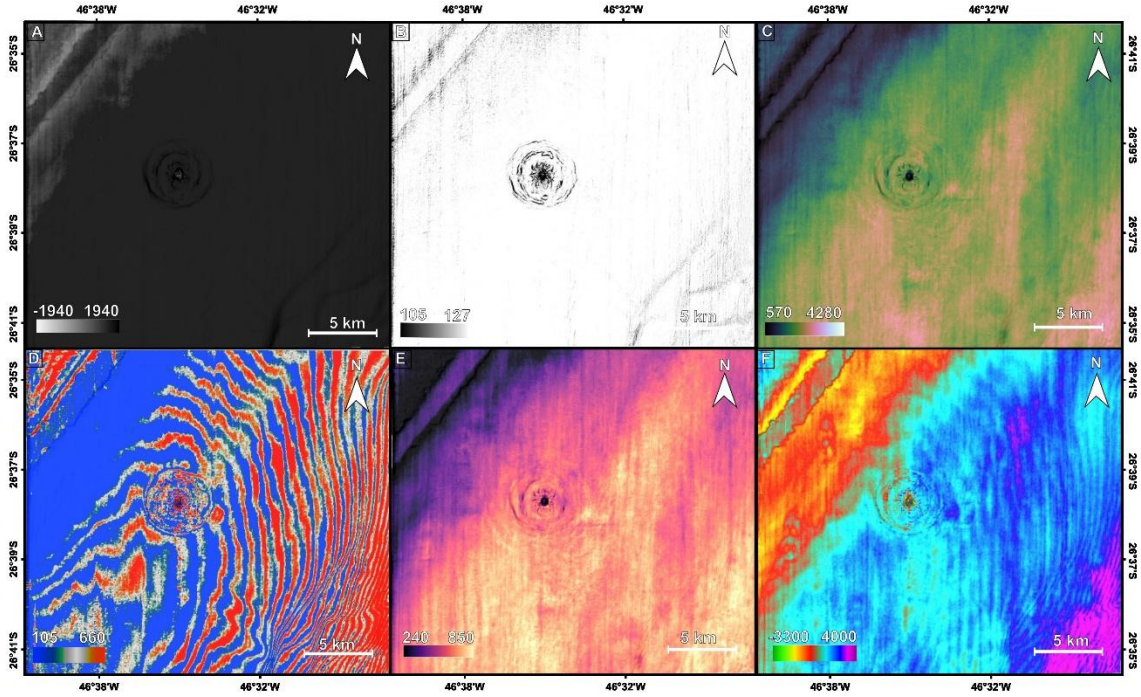


Figure 31. Composite maps from a horizon slice near the top of the structure designated as H3 horizon slice (A, seismic section without attributes) and its seismic attributes: coherence cube (B), RMS amplitude (C), relief (D), sweetness (E), and relative acoustic impedance (F).

6.2 Praia Grande structure

6.2.1 Seismic-stratigraphic and structural framework

Figure 32 presents a comparative display of two 2D vertical seismic sections oriented West-to-East (W-E). The upper section exhibits the original seismic data (in grayscale amplitude), while the lower section presents the detailed stratigraphic and structural interpretation of a complex impact crater. In the Praia Grande impact structure, six seismic horizons were interpreted, Santonian, D1 unconformity, Turonian, Albian, Top of salt, and Base of salt. Note the central uplift, visible as a central elevation of the Turonian horizon in green, which is characteristic of complex impact structures.

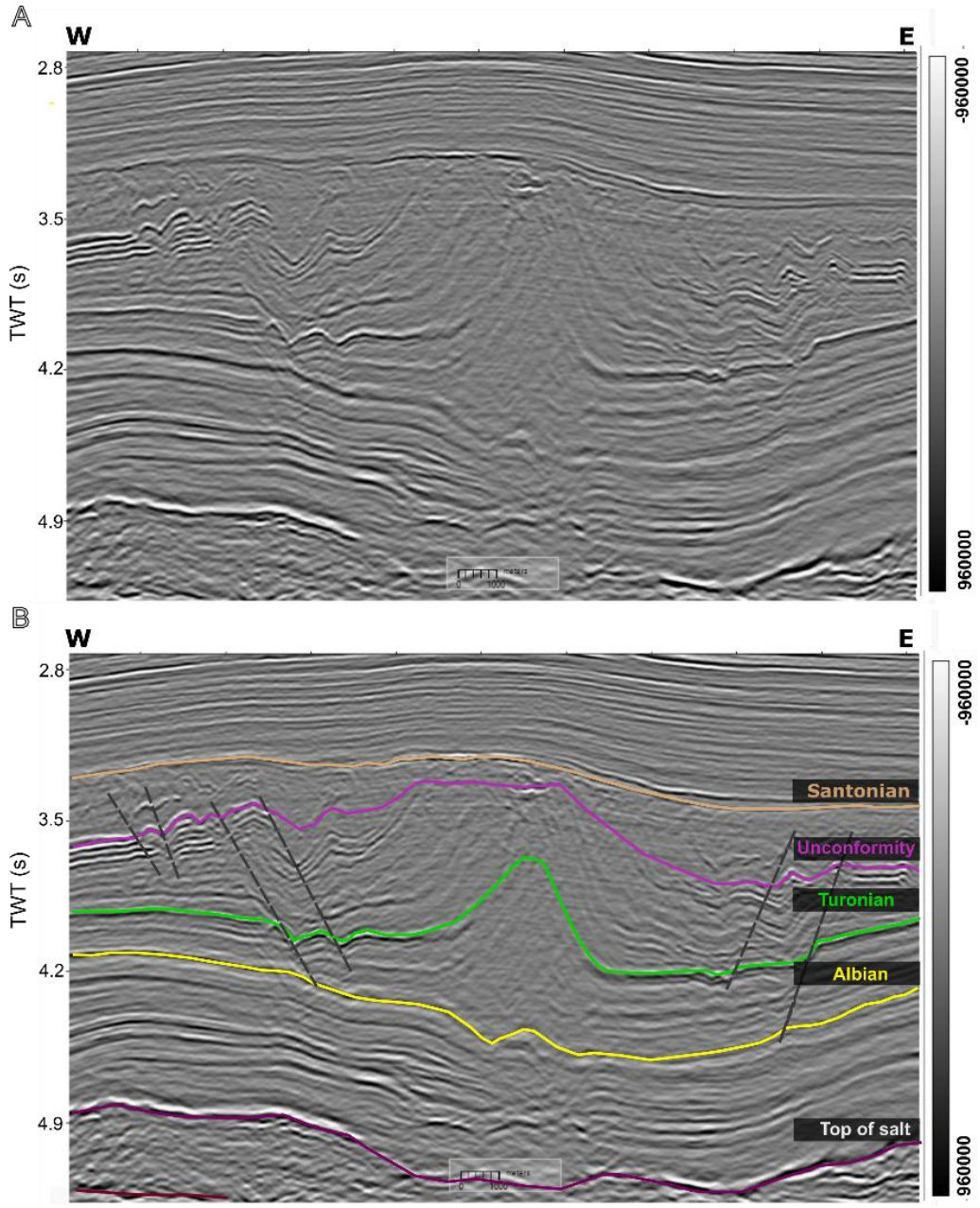


Figure 32. Seismic Inline 1726 (time) across the Praia Grande impact structure showing the interpreted horizons (Santonian, D1 unconformity, Turonian, Albian, Top of salt, and Base of salt) and the mapped faults.

The Top of Salt, located near the two-way travel time of 4.9 s, maps the top of the deep evaporitic layer that serves as the structural substrate (Figure 32). The corresponding Albian reflector (Lower Cretaceous), highlighted in yellow, is severely deformed, exhibiting pronounced subsidence and flexural warping beneath the crater floor. The Turonian horizon (in green) marks a major unconformity and the syn-impact infill; it clearly outlines the classic morphology of a complex impact crater, featuring a

deep annular collapse trough along the flanks and a highly prominent central uplift that reaches approximately 3.6 s. Marked in magenta is an erosional or truncation surface that partially seals the rugged topography left immediately after the crater modification stage. Located at around 3.3 s, the Santonian horizon represents the post-impact deposition (Upper Cenomanian to Santonian).

Furthermore, the relief seismic attribute was fundamental in visualizing the faults. For instance, figure 33 clearly highlights these discontinuities within the seismic section. This seismic attribute creates a visual effect of shading and three-dimensional relief on the 2D image, making the peaks and troughs much more textured.

In the central portion of the image (horizontally between the center and slightly to the right, at a depth of 3.6 s), a massive zone of chaotic seismic facies and loss of linear reflectivity is observed. This corresponds to the uplifted central peak, where the violent elastic rebound of the impact fractured and mixed deep rock blocks, destroying the original continuity of the layers.

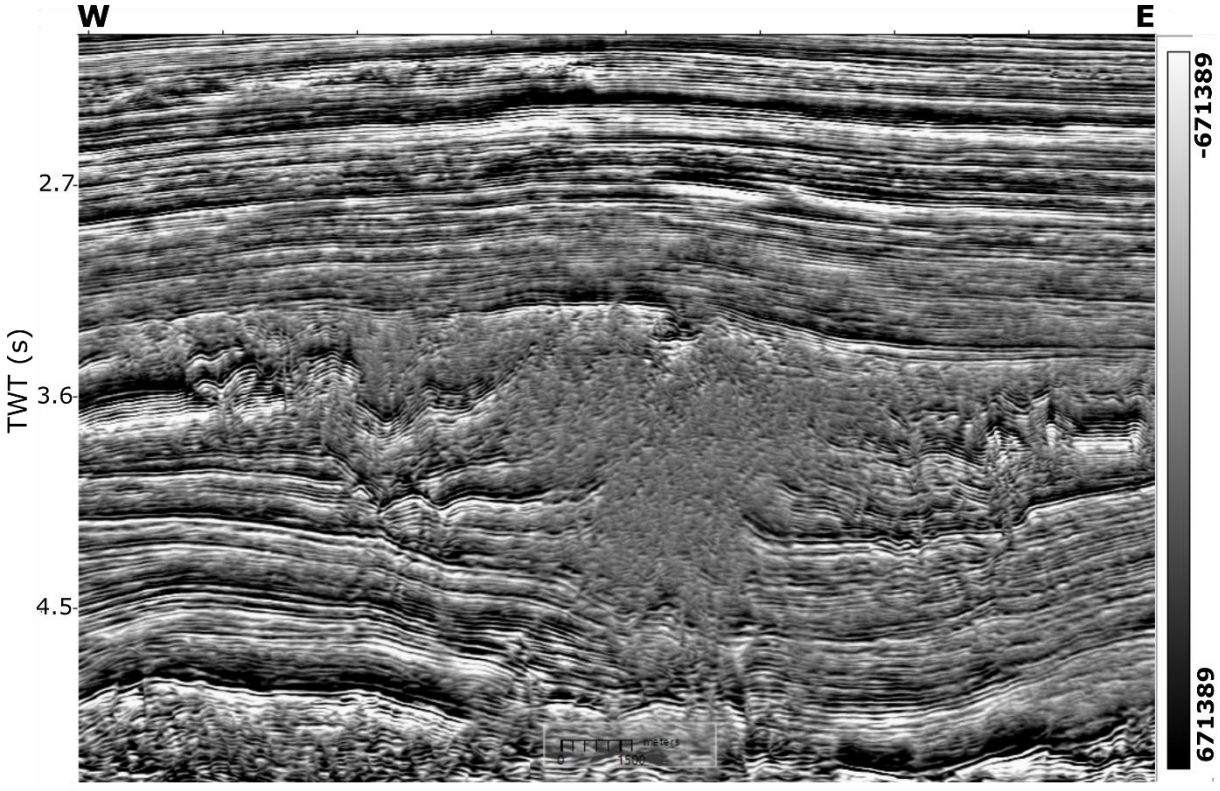


Figure 33. Seismic Inline 1726 (time) processed with Relief seismic attribute, aiming to highlight structural features and stratigraphic discontinuities within Praia Grande impact crater area.

6.2.2 Mapped horizons

Figure 34 presents a structural time map (structural contour grid) of the surface corresponding to the Santonian horizon, generated from 3D seismic data. The map utilizes a rainbow color scale to represent depth variations in two-way travel time. Warmer colors correspond to shorter two-way travel times, indicating shallower areas, while cooler colors represent deeper regions. The grid reveals the subtle topographic expression that the impact crater still exerted during the deposition or accommodation of the Santonian sediments.

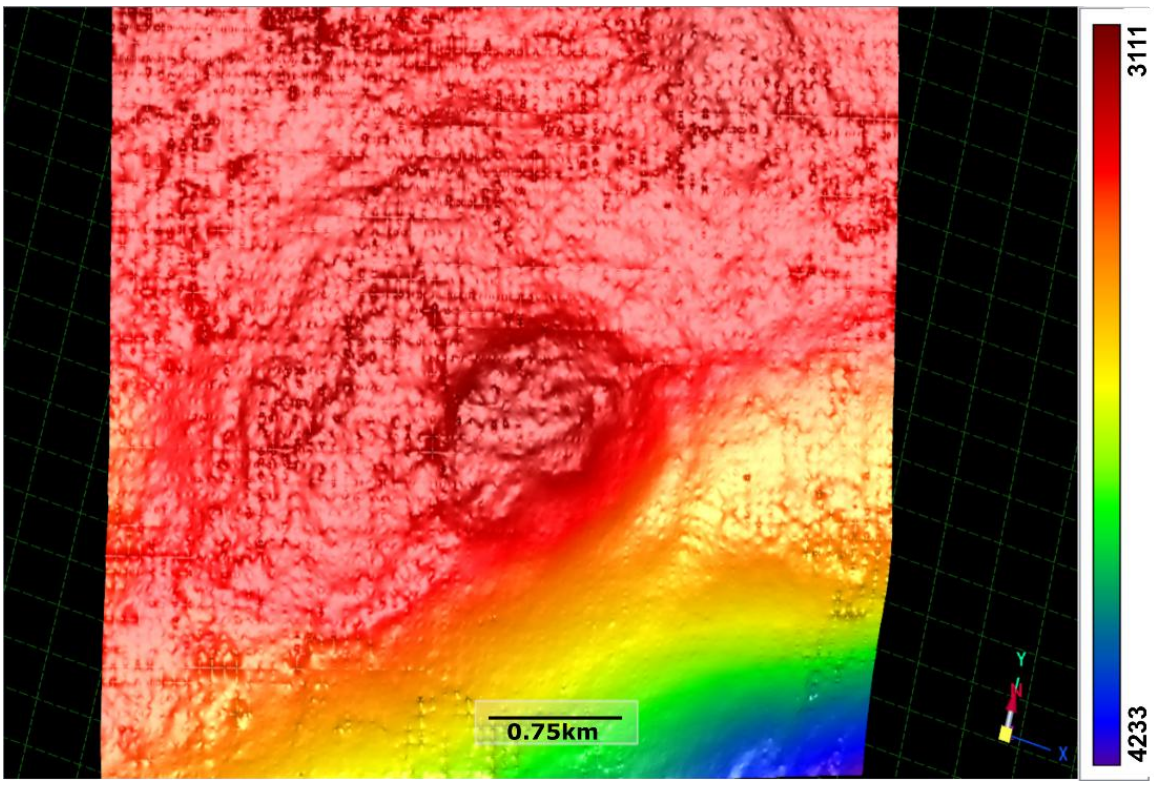


Figure 34. Santonian horizon slice in time. The color scale represents two-way travel time (ms), with warmer colors indicating shorter travel times (shallower areas) and cooler colors indicating longer travel times (deeper areas). Red corresponds to approximately 3111 ms, whereas blue corresponds to approximately 4233 ms.

Figure 35 shows the D1 unconformity horizon slice displayed with the coherence cube attribute. At the center of the block, a circular area densely populated by intricate

black lineaments is observed. This highly chaotic texture reflects the central uplift or the internal collapse zone of the crater, where a severe loss of seismic coherence highlights intense rock fracturing. Areas of low coherence, expressed as dark zones, correspond to faulted regions and the central anticline. The ring faults are clearly visible. Surrounding the central core, the attribute accurately highlights a circular geometric pattern of concentric black lineaments. These lines map the physical discontinuities within the rock, visually delineating the fault scarps and structural terraces generated by the collapse of the crater rims.

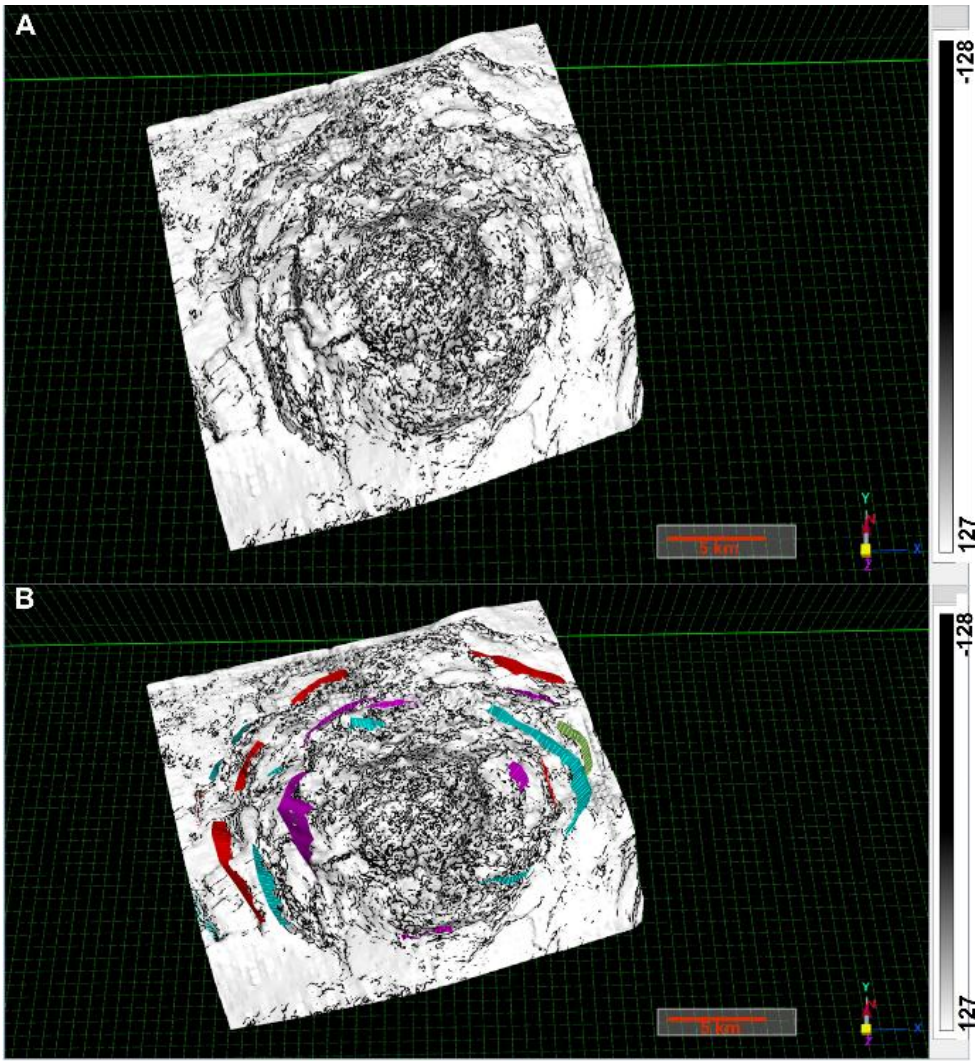


Figure 35. 3D view of the Horizon Slice D1 Unconformity processed with a seismic coherence attribute (grayscale) highlighting the structural expression of the impact crater. (A) Uninterpreted surface displaying a highly chaotic central core corresponding to the central uplift, surrounded by distinct concentric black lineaments that mark physical discontinuities and fault scarps. (B) Interpreted structural framework displaying 3D fault planes (colored blades in red, magenta, light blue, and green) tracking the concentric lineaments, illustrating the listric normal ring fault systems developed during the crater modification stage. Note the 5 km scale bar for regional dimensioning.

Figure 36 presents a three-dimensional structural map (Turonian grid surface) derived from seismic data, illustrating the morphology of complex impact crater. Exactly at the center of the structure, a prominent, peaked feature stands out, rising significantly above the crater floor. On the color map, the top of this central peak reaches the shallowest elevations (dark red tones).

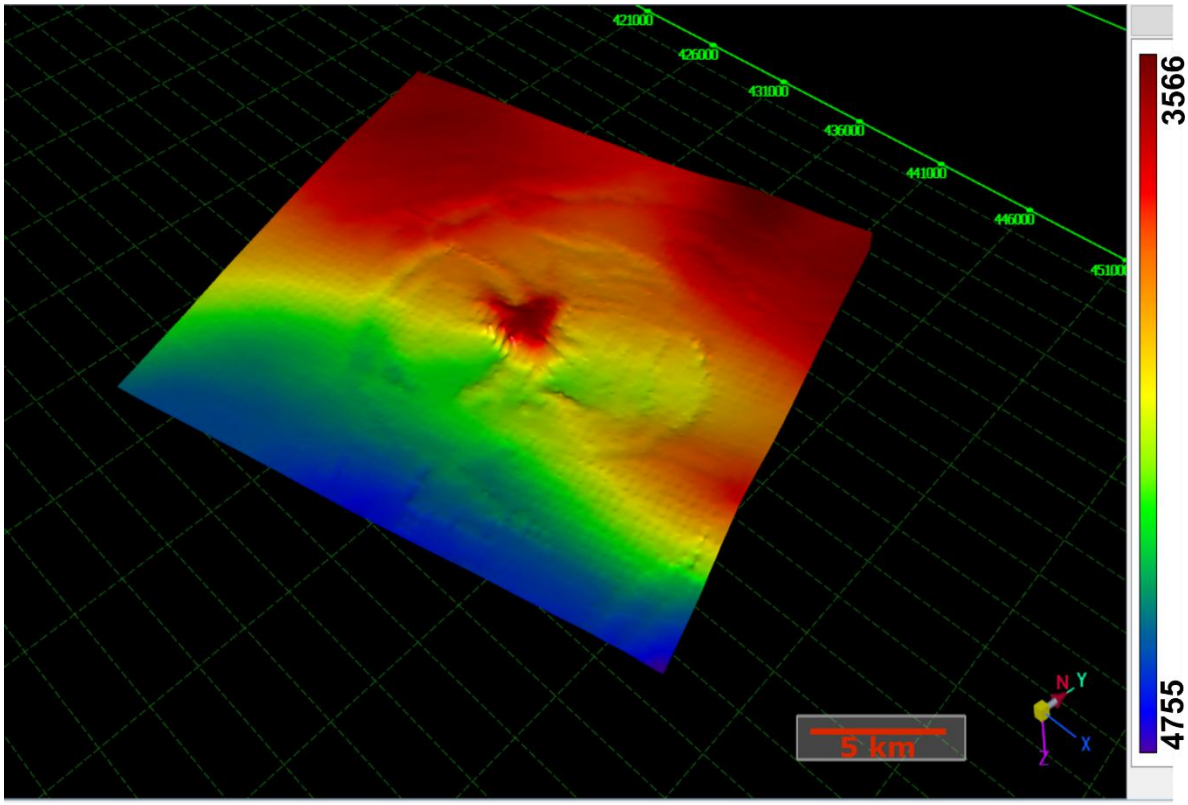


Figure 36. Turonian horizon slice. The color scale represents two-way travel time (ms), with warmer colors indicating shorter travel time (shallower areas) and cooler colors indicating longer travel times (deeper areas). Red corresponds to approximately 3566 ms, whereas blue corresponds to approximately 4755 ms.

The coherence cube attribute (Figure 37) highlights zones of low coherence associated with the impact structure. In addition, linear features are observed in the horizon slice. The origin of these features is uncertain and they may reflect either attribute-related effects or interpretation-related artifacts. Therefore, they are not considered as definitive geological structures in this study.

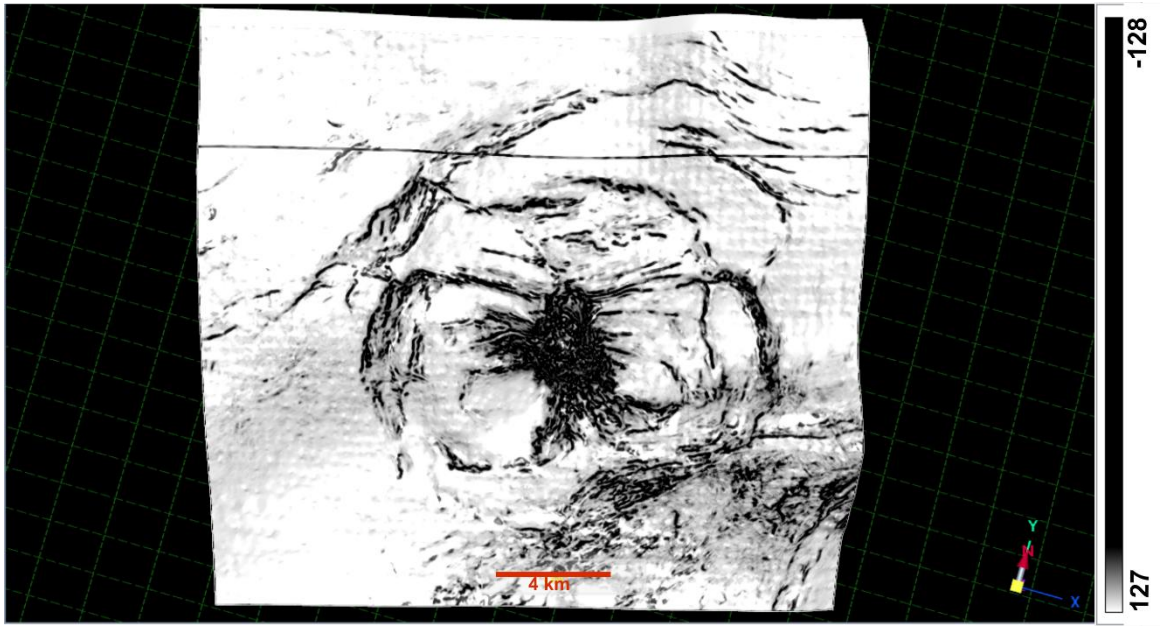


Figure 37. Turonian horizon slice displayed with the coherence cube attribute. Darker colors indicate lower coherence values.

Figure 38 shows the Albian horizon slice, located below the base of the crater. The circular geometry of the crater is still visible at this deeper level, although less pronounced than in the overlying horizons. Some localized disruptions in the reflectors can be observed, which may correspond to extensions of the fault network.

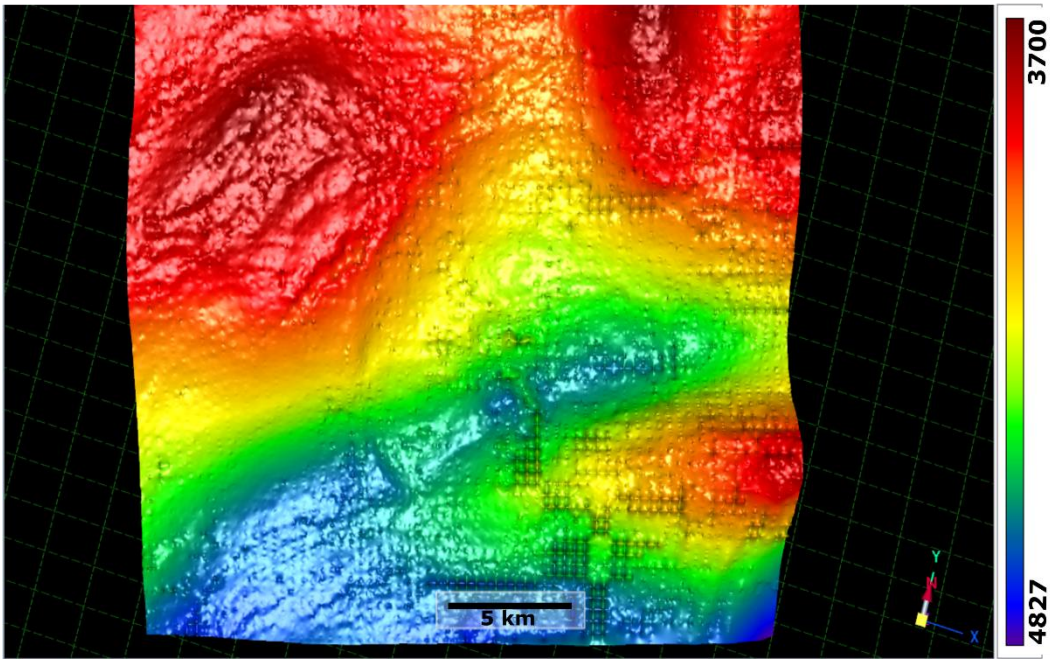


Figure 38. Albian horizon slice. The color scale is in two-way travel time (ms), with red representing shallower areas (~3700 ms) and blue representing deeper areas (~4827 ms).

7. Discussion

7.1 Geometry and structural interpretation

The seismic interpretation of the Ilha do Mel and Praia Grande structures revealed characteristic features of complex impact craters, including concentric normal faults, central uplift, and localized circular depressions. At Ilha do Mel, the fault network is best expressed in the H1 horizon, where coherence cube analysis clearly delineates the annular fault pattern, while deeper horizons (H2 and H3) show the same pattern less prominently. Smaller circular features surrounding the central zone may represent secondary impact structures or zones of localized deformation.

The geometric analysis of the layers of the Praia Grande impact structure allows dating the impact event to the Turonian based on stratigraphic criteria. Deformation of the pre-impact layers likely occurred from the Albian to the Turonian. In Figure 32, the Albian (yellow) and lower/middle Turonian (green) layers were directly impacted, undergoing listric normal faulting and severe fracturing (indicated by the dashed gray lines along the crater rims). At the center, the Turonian (green) underwent a violent mechanical rearrangement that pushed the rocks upward, forming the central uplift. This proves that these units already existed at the moment of collision. The geometry of the Santonian horizon (orange) provides post-impact evidence, as it exhibits a drastic geometric behavior of onlap and thinning. It gently follows and 'envelopes' the crest of the central uplift, becoming significantly thinner over the top of the peak than in the adjacent annular basins.

This stratigraphic thinning at the center demonstrates differential subsidence and the infilling of a pre-existing topography. The impact created the subaqueous relief (the central peak) during the Turonian; subsequently, the Santonian sediments accommodated over this topographic barrier, depositing less material on the top and more material within the depressed flanks. Therefore, the Santonian sedimentary infill postdates the impact.

The attributes RMS amplitude and sweetness produced similar results in highlighting the main horizons (H1, H2, and H3) of the Ilha do Mel structure (Figures 29-31). Although the coherence cube generated an artifact in Figure 37, it proved to

be the most effective attribute for delineating the concentric fault patterns of the impact structures. Overall, combining multiple seismic attributes enabled a more robust interpretation of crater morphology and structural framework, underscoring the value of attribute analysis in buried impact structures.

The mapped morphology of the studied structures is consistent with that of complex impact craters, as they exceed 4 km in diameter and display a central uplift surrounded by concentric normal faults. A comparable example is the Nadir Crater (Figure 6), located offshore West Africa, which represents a candidate Cretaceous-Paleogene impact structure and exhibits similar morphological characteristics, including a central uplift and annular normal fault systems.

8. Conclusions

The primary contribution of this research is the application and evaluation of seismic attributes to identify buried impact craters. Based on the analysis of the Ilha do Mel and Praia Grande structures, the coherence cube proved to be the most effective attribute for delineating the concentric normal faults associated with these features. Although an impact origin for both structures has not yet been conclusively confirmed—due to the lack of wells fully penetrating the features to provide direct evidence of shock metamorphism, such as planar deformation features (PDFs) in quartz—their mapped morphologies are entirely consistent with complex impact craters. These diagnostic characteristics include a central uplift and concentric, circular normal faults interpreted as products of post-impact collapse processes. Furthermore, this study contributes to the chronological framework of the region by constraining the age of the Praia Grande structure to the Turonian rather than the Santonian, as suggested in previous literature. Seismic attribute analysis was essential for mapping these structural elements, highlighting acoustic impedance contrasts and lithological variations within the crater zones. Consequently, future drilling campaigns targeting these target zones are required to provide definitive confirmation of their impact origin.

REFERENCES

Agência Nacional do Petróleo, Gás Natural e Biocombustíveis (ANP). Boletim Mensal da Produção de Petróleo e Gás Natural. Out, 2025. Rio de Janeiro, 2025. Disponível em: https://www.gov.br/anp/pt-br/centrais-de-conteudo/publicacoes/boletins-anp/arquivos-bmppgn/2025/outubro.pdf. Accessed December 5, 2025.

Alvarez, L. W., Alvarez, W., Asaro, F., & Michel, H. V. (1980). Extraterrestrial cause for the Cretaceous-Tertiary extinction. *Science*, *208*(4448), 1095-1108.

Anstey, N. 2005. Attributes in color: the early years. *CSEG Recorder*, *30*(3), 12-15.

Armour, M. H., Boyce, J. I., Shulman, Z., & Zilkey, D. R., 2024. 3-D geophysical modeling of a buried, simple impact crater: Holleford impact structure, Ontario, Canada. *Meteoritics & Planetary Science*, *59*(1), 171-192.

Avona, P. D., Crósta, A. P., Vasconcelos, M. A. R., Bjonnes, E., Pereira, F. L., & Góes, A. M., 2025. Geology, gravity, and numerical modeling of the Nova Colinas impact structure, Parnaíba Basin, Brazil. *Meteoritics & Planetary Science*, *60*(2), 286-307.

Balch, A. H. 1971. Color sonagrams: A new dimension in seismic data interpretation. *Geophysics*, *36*(6), 1074-1098.

Baptista, R. J., Ferraz, A. E., Sombra, C., dos Santos Neto, E. V., Plawiak, R., Lops Silva, C. L., ... & Gamboa, L. A. P. 2023. The presalt Santos Basin, a super basin of the twenty-first century. *AAPG Bulletin*, *107*(8), 1369-1389.

Barboza, H. R., 2025. Inversão sísmica elástica e caracterização do reservatório do sistema turbidítico do Campo de Atlanta, pós-sal da Bacia de Santos. Master's Dissertation. Universidade Federal Fluminense. Niterói, RJ.

Barnes, A. E. 2001. Seismic attributes in your facies. *CSEG recorder*, *26*(7), 41-47.

Barnes, A. E., 2016. Handbook of Poststack Seismic Attributes. In *Handbook of Poststack Seismic Attributes*. https://doi.org/10.1190/1.9781560803324

Bodén, A., & Erikson, K. G. (1988). Deep Drilling in Crystalline Bedrock; Vol. 1: The Deep Gas Drilling in the Siljan Impact Structure, Sweden and Astroblemes. In *Proceedings of the International Symposium. Springer Verlag, Berlin*.

Bulhões, É. M. 1999, August. Técnica “VOLUME DE AMPLITUDE” para mapeamento de feições estruturais. In *6th International Congress of the Brazilian Geophysical Society* (pp. cp-215). European Association of Geoscientists & Engineers.

Bulhões, É. M., & de Amorim, W. N., 2005. Princípio da SismoCamada Elementar e sua aplicação à Técnica Volume de Amplitudes (tecVA). In *9th International Congress of the Brazilian Geophysical Society* (pp. cp-160). European Association of Geoscientists & Engineers.

Cainelli, C., & Mohriak, W. U. 1999. Some remarks on the evolution of sedimentary basins along the Eastern Brazilian continental margin. *Episodes Journal of International Geoscience*, *22*(3), 206-216.

Carlotto, M. A., da Silva, R. C. B., Yamato, A. A., Trindade, W. L., Moreira, J. L. P., Fernandes, R. A. R., ... & da Silva-Telles, A. C. 2017. Libra: A newborn giant in the Brazilian Presalt Province.

Carpenter, B. N., & Carlson, R. 1997. The Ames meteorite-impact crater. *Ames structure in northwest Oklahoma and similar features: origin and petroleum production*, *100*, 104-119.

Castro, T. M., 2019. *Avaliação dos reservatórios carbonáticos do pré-sal no Campo de Búzios, Bacia de Santos* (Master thesis, Universidade Federal Fluminense).

Chang, H. K., Assine, M. L., Corrêa, F. S., Tinen, J. S., Vidal, A. C., & Koike, L. 2008. Sistemas petrolíferos e modelos de acumulação de hidrocarbonetos na Bacia de Santos. *Brazilian Journal of Geology*, *38*(2), 29-46.

Chen, Q., & Sidney, S., 1997. Seismic attribute technology for reservoir forecasting and monitoring. *The Leading Edge*, *16*(5), 445-448.

Chopra, S., Castagna, J., & Xu, Y., 2009. Relative acoustic impedance application for thin-bed reflectivity inversion. In *SEG Technical Program Expanded Abstracts 2009* (pp. 3554-3558). Society of Exploration Geophysicists.

Chopra, S., & Marfurt, K. J. 2005. Seismic attributes—A historical perspective. *Geophysics*, *70*(5), 3SO-28SO.

Chopra, S., & Marfurt, K. J. 2007. *Seismic attributes for prospect identification and reservoir characterization*. Society of Exploration Geophysicists and European Association of Geoscientists and Engineers.

Correia, G. A., de Menezes, J. R. C., Bueno, G. V., & Marques, E. J. J., 2005. Identificação de uma estrutura de impacto no Cretáceo Superior da Bacia de Santos em sísmica de reflexão 3D. *Boletim de Geociências da Petrobras*, *13*(1), 123-127.

Crosta, A. P., Kazzuo-Vieira, C., Choudhuri, A., & Schrank, A. 2005. Astroblema Domo de Vargeão, SC-Registro de impacto meteorítico sobre rochas vulcânicas da bacia do Paraná. *Winge, M.; Schobbenhaus, C.; Berbert-Born, M*.

Crosta, A. P., 2024. Registros geológicos de impactos meteoríticos no Brasil: evolução e estágio atual. *Derbyana*, *45*.

Dence, M. R., 1972. The Nature and significance of terrestrial impact structures, *24th Int. Geol. Congr.*, 77-89.

Emujakporue, G. O., & Enyenihi, E. E. (2020). Identification of seismic attributes for hydrocarbon prospecting of Akos field, Niger Delta, Nigeria. *SN Applied Sciences*, *2*, 1-11.

Ferreira, D. J. A., 2018.*Classificação de sismofácies utilizando multi-atributos sísmicos aplicadas em reservatórios carbonáticos no pré-sal da Bacia de Santos* (Master thesis, Universidade Federal Fluminense).

French, B. M., 1998. *Traces of catastrophe: A handbook of shock-metamorphic effects in terrestrial meteorite impact structures* (No. LPI-Contrib-954).

Glikson, A., & Uysal, I. T., 2013. Geophysical and structural criteria for the identification of buried impact structures, with reference to Australia. *Earth-Science Reviews*, *125*, 114-122.

Grajales-Nishimura, J. M., Cedillo-Pardo, E., Rosales-Domínguez, C., Morán-Zenteno, D. J., Alvarez, W., Claeys, P., ... & Sánchez-Ríos, A. 2000. Chicxulub impact: The origin of reservoir and seal facies in the southeastern Mexico oil fields. *Geology*, *28*(4), 307-310.

Grieve, R. A. 2005. Economic natural resource deposits at terrestrial impact structures.

Gulick, S. P. S., Christeson, G. L., Barton, P. J., Grieve, R. A. F., Morgan, J. V., & Urrutia-Fucugauchi, J., 2013. Geophysical characterization of the Chicxulub impact crater. *Reviews of Geophysics*, *51*(1), 31-52.

Hart, B. S., 2008. Channel detection in 3-D seismic data using sweetness. *AAPG bulletin*, *92*(6), 733-742.

Juhlin, C., Sturkell, E., Ebbestad, J. O. R., Lehnert, O., Högström, A. E., & Meinhold, G. (2012). A new interpretation of the sedimentary cover in the western Siljan Ring area, central Sweden, based on seismic data. *Tectonophysics*, *580*, 88-99.

Kearey, P., Brooks, M., & Hill, I. (2002). *An introduction to geophysical exploration* (Vol. 4). John Wiley & Sons.

Kelly, A. O., & Dachille, F. (1953). *Target: Earth: The role of large meteors in earth science*. Target: Earth.

Kenkmann, T., 2021. The terrestrial impact crater record: A statistical analysis of morphologies, structures, ages, lithologies, and more. *Meteoritics & Planetary Science*, *56*(5), 1024-1070.

Magoon, L. B., & Dow, W. G. 1994. The petroleum system.

Marfurt, K. J. 2018. Chapter 2, Seismic Attributes and What They Measure. *Distinguished Instructor Series: Seismic Attributes as the Framework for Data Integration Throughout the Oilfield Life Cycle, SEG Books*, 25-150.

Mazur, M. J., Stewart, R. R., & Hildebrand, A. R., 2000. The seismic signature of meteorite impact craters. *CSEG Recorder*, *25*(6), 10-16.

Milani, E. J., Brandão, J. A. S. L., Zalán, P. V., & Gamboa, L. A. 2000. Petróleo na margem continental brasileira: geologia, exploração, resultados e perspectivas. *Revista Brasileira de Geofísica*, *18*(3), 352-396.

Menezes, J. R. C., Rodrigues, J. J. G., Rodrigues, L. F., & de Vasconcelos, C. S., 2012. A estrutura de impacto Ilha do Mel: Um novo astroblema em sísmica 3D na Bacia de Santos.

Moreira, J.L.P., Madeira, C.V., Gil, J.A., Machado, M.A.P., et al., 2007. Bacia de Santos. Bol. Geocienc. PETROBRAS 15 (2), 531–549.

Mohriak, W., Nemčok, M., & Enciso, G. 2008. South Atlantic divergent margin evolution: rift-border uplift and salt tectonics in the basins of SE Brazil.

Nicholson, U., Bray, V. J., Gulick, S. P., & Aduomahor, B., 2022. The Nadir crater offshore West Africa: A candidate cretaceous-paleogene impact structure. *Science Advances*, *8*(33), eabn3096.

Nicholson, U., Jonge-Anderson, I. D., Gillespie, A., Kenkmann, T., Dunkley Jones, T., Collins, G. S., ... & Parr, R., 2025. Multiple lines of evidence for a hypervelocity impact origin for the Silverpit Crater. *Nature Communications*, *16*(1), 8312.

Osinski, G. R., 2004. *Hypervelocity impact into sedimentary targets: Processes and products,* PhD Thesis, University of New Brunswick.

Osinski, G. R., 2006. The geological record of meteorite impacts. In *Proc 1st Int Conf Impact Cratering in the Solar System* (pp. 8-12).

Pilkington, M., & Grieve, R. A. F., 1992. The geophysical signature of terrestrial impact craters. *Reviews of Geophysics*, *30*(2), 161-181.

Pereira, F. L., Crosta, A. P., Avona, P. D., Vasconcelos, M. A. R., & Goés, A. M., 2024. Magnetometric and seismic investigation of the Nova Colinas impact structure, Parnaíba Basin, Brazil. *Journal of South American Earth Sciences*, *149*, 105215.

Pereira, M. J., & Feijó, F. J. 1994. Bacia de Santos. *Boletim de Geociências da PETROBRAS*, *8*(1), 219-234.

Pierazzo, E., Hahmann, A. N., Sloan, L. C. 2003. *Astrobiology* 3, 99.

Pietzsch, R., Oliveira, D. M., Tedeschi, L. R., Neto, J. V. Q., Figueiredo, M. F., Vazquez, J. C., & de Souza, R. S. 2018. Palaeohydrology of the Lower Cretaceous pre-salt lacustrine system, from rift to post-rift phase, Santos Basin, Brazil. *Palaeogeography, Palaeoclimatology, Palaeoecology*, *507*, 60-80.

Neto, E. R. O. 2019. *Controle dos Corpos Ígneos na Deposição de Corpos Turbidíticos do Santoniano no Campo de Uruguá, Bacia de Santos* (Undergraduate thesis, Universidade Federal Fluminense).

Reynolds, J. M. 2011. *An introduction to applied and environmental geophysics*. John Wiley & Sons.

Santos, L. A., Neves, E. H. P., Freire, A. F. M., Santos, M. A. C., Matsumoto, R., & Ajus, C. M. (2020). Diffraction velocity analysis in a single-channel seismic survey in the Joetsu Basin. *Geophysics*, *85*(2), U47-U53.

Schulte, P., Alegret, L., Arenillas, I., Arz, J. A., Barton, P. J., Bown, P. R., ... & Willumsen, P. S., 2010. The Chicxulub asteroid impact and mass extinction at the Cretaceous-Paleogene boundary. *Science*, *327*(5970), 1214-1218.

Schulte, B. 2012. Overview on the Fundamentals of Imaging. *CSEG Recorder*, *37*, 40.

Scotese, C. R., Song, H., Mills, B. J., & van der Meer, D. G. 2021. Phanerozoic paleotemperatures: The earth's changing climate during the last 540 million years. *Earth-Science Reviews*, *215*, 103503.

Sheriff, R. E., & Geldart, L. P. 1995. *Exploration seismology*. Cambridge university press.

Siqueira, R., Fetter, M., & Cetale, M., 2024. Structural geology and deformation analysis in the Búzios-Itapu area, Santos Basin—offshore Brazil. *Journal of South American Earth Sciences*, *134*, 104779.

Simm, R., & Bacon, M. 2014. *Seismic amplitude: An interpreter's handbook*. Cambridge university press.

Taner, M. T., Koehler, F., & Sheriff, R. E. 1979. Complex seismic trace analysis. *Geophysics*, *44*(6), 1041-1063.

Taner M. T., 2001 Seismic attributes: Canadian Society of Exploration Geophysicists Recorder 26(9):48–56

Telford, W. M., Geldart, L. P., & Sheriff, R. E. 1990. *Applied geophysics*. Cambridge university press.

Texeira, C. C., Siqueira, C. Y. S., Aquino Neto, F. R., Miranda, F. P., Cerqueira, J. R., Vasconcelos, A. O., ... & Herrera, M. (2014). Source identification of sea surface oil with geochemical data in Cantarell, Mexico. *Microchemical Journal*, 117, 202-213. https://doi.org/10.1016/j.microc.2014.06.025

Toon, O. B., Zahnle, K., Morrison, D., Turco, R. P., Covey, C. 1997. *Rev. Geophys.* 35, 41

Vasconcelos, M. A. R., 2007. *Caracterização geofísica da estrutura de impacto de Araguainha, MT/GO* (Master thesis, Universidade de São Paulo).

Vernengo, L., & Trinchero, E. (2015). Application of amplitude volume technique attributes, their variations, and impact. *The Leading Edge*, *34*(10), 1246-1253.

Viana, R. P. C., 2018. *Impactos da halocinese na interpretação sísmica em uma porção distal da Bacia de Santos* (Master thesis, Universidade Federal Fluminense).

Wright, V. P., & Barnett, A. J. 2015. An abiotic model for the development of textures in some South Atlantic early Cretaceous lacustrine carbonates.

Yilmaz, Ö. 2001. *Seismic data analysis: Processing, inversion, and interpretation of seismic data*. Society of exploration geophysicists.

Zoeppritz, K. 1919. Uber reflexion und durchgang seismischer wellen durch Unstetigkerlsflaschen. *Berlin, Uber Erdbebenwellen VII B, Nachrichten der Koniglichen Gesellschaft der Wissenschaften zu Gottingen, math-phys. K1*, (57), 84.

Zucolotto, M. Elizabeth; Fonseca, Ariadne do Carmo; Antonello, Loiva Lízia., 2013. Decifrando os meteoritos.